

KRAMER-PESCH EFFECT IN $\text{LuNi}_2\text{B}_2\text{C}$

by

ASTRIA PRICE

BE (Hons), The University of Melbourne, 1994

BSc (Hons), The University of Melbourne, 1996

A THESIS SUBMITTED IN PARTIAL FULFILLMENT OF
THE REQUIREMENTS FOR THE DEGREE OF

MASTER OF SCIENCE

in

THE FACULTY OF GRADUATE STUDIES

DEPARTMENT OF PHYSICS AND ASTRONOMY

We accept this thesis as conforming
to the required standard

THE UNIVERSITY OF BRITISH COLUMBIA

October 2001

© Astria Price, 2001

In presenting this thesis in partial fulfillment of the requirements for an advanced degree at the University of British Columbia, I agree that the Library shall make it freely available for reference and study. I further agree that permission for extensive copying of this thesis for scholarly purposes may be granted by the head of my department or by his or her representatives. It is understood that copying or publication of this thesis for financial gain shall not be allowed without my written permission.

Department of Physics and Astronomy

The University of British Columbia
Vancouver, Canada

Date 12 OCTOBER 2001

Abstract

This thesis describes μ SR observations of the internal magnetic field distribution $n(B)$ as a function of temperature in $\text{LuNi}_2\text{B}_2\text{C}$ ($T_c = 16.0$ K, $H_{c2}(0) = 7$ T), under a magnetic field of $H = 1.2$ T applied parallel to the crystal \hat{c} axis. The μ SR polarisation signal is fitted to a nonlocal London model, assuming a square vortex lattice. By incorporating first order nonlocal corrections, this model achieves significantly better fits than the local London model. The fitted penetration depth temperature dependence $\lambda(T)$ follows the form expected for a BCS s -wave superconductor, although the dependence is also consistent with a slight linear increase in the penetration depth λ with rising temperature. The rate of any such linear growth, however, is smaller than would be expected for an energy gap Δ with line nodes. The fitted core radius temperature dependence $\rho(T)$ reveals a Kramer-Pesch effect, or linear contraction of the vortex core radius ρ upon cooling at low temperatures $T \ll T_c$, that is weaker than predicted. The Kramer-Pesch effect found for this nearly three-dimensional superconductor is almost identical to that seen in quasi two-dimensional NbSe_2 , implying that quasiparticles behave similarly in $\text{LuNi}_2\text{B}_2\text{C}$ and NbSe_2 despite their different dimensionalities, and that longitudinal disorder of vortices has negligible impact on μ SR determinations of the vortex core radius ρ . The surprisingly small magnitude of the Kramer-Pesch effect suggests that future theoretical work on the temperature dependence of vortex structure should consider zero point motion of vortices and intervortex interactions.

Contents

Abstract	ii
List of Tables	v
List of Figures	vi
Acknowledgements	viii
1 Introduction	1
2 Superconductivity	4
2.1 London Theory	4
2.2 BCS Theory	7
2.3 Ginzburg-Landau Theory	8
2.4 The Vortex Core	11
3 Material Properties of LuNi₂B₂C	13
3.1 The Nickel Borocarbide Family	13
3.2 LuNi ₂ B ₂ C	15

<i>CONTENTS</i>	iv
4 Experiment	18
4.1 Transverse Field μ SR	18
4.2 Apparatus Setup	19
5 Analysis	24
5.1 Data Fitting in the Time Domain	24
5.2 Model for the Internal Field Distribution	25
5.3 Fitting Software	28
5.4 Calculation of the Core Radius	31
5.5 Fit Quality	34
6 Results and Discussion	40
7 Conclusions	47
Bibliography	49

List of Tables

3.1	LuNi ₂ B ₂ C interatomic distances	15
5.1	Number of data points analysed	37
6.1	Fitted parameters and internal field distributions $n(B)$	42

List of Figures

1.1	Type I and II superconductivity	2
2.1	Field decay below the surface of a superconductor in the Meissner state	5
2.2	Boundary between normal and superconducting regions	10
3.1	RNi ₂ B ₂ C crystal structure	14
4.1	Experimental setup	20
4.2	Positron detector arrangement	22
5.1	Expected nonlocality parameter $C(T)$	27
5.2	Sampling the vortex lattice	29
5.3	Fitted internal field $B(\mathbf{r})$	32
5.4	Supercurrent density $J(r)$ and core radius ρ	33
5.5	Fitted muon spin precession signal $\tilde{P}(t)$	35
5.6	Variation of χ^2/n with penetration depth λ	36
5.7	Variation of χ^2/n with nonlocality parameter C	38
5.8	Variation of χ^2/n with core radius ρ	39

LIST OF FIGURES

vii

6.1	Measured penetration depth $\lambda(T)$ and nonlocality parameter $C(T)$. .	41
6.2	Fitted internal field distribution $n(B)$	43
6.3	Measured core radius $\rho(T)$	45

Acknowledgements

I would like to thank Rob Kiefl for his excellent supervision of the work which led to this thesis, his steady stream of advice, and his continual encouragement and support. He, Jeff Sonier and Roger Miller taught me how to fit μ SR superconductivity data to a theoretical model. They, together with Sarah Dunsiger, Jacques Chakhalian, Gerald Morris, Jess Brewer and the TRIUMF technical staff, including Mel Good and Bassam Hitti, assisted greatly in the setup and running of the experiment described in this thesis. They also answered my many questions about the μ SR technique. Paul Canfield provided the sample studied in this experiment. I thank Jess Brewer additionally for giving this thesis its second reading, and am grateful to the Canadian Institute of Advanced Research for enabling me to meet with numerous researchers in the field of superconductivity.

Chapter 1

Introduction

Superconductivity refers to the unusual electrical and magnetic behaviour exhibited by certain materials below their critical temperature T_c , usually near absolute zero. These phenomena include negligible resistance to electric current and the expulsion of external magnetic fields, and find application in Magnetic Resonance Imaging (MRI) and high capacity power transmission cables. Based on their response to the applied magnetic field H , superconductors fall into two major classes, type I and type II, as illustrated in Figure 1.1. A type I superconductor exhibits the Meissner effect, the exclusion of the magnetic field from its interior, at an applied field H below its thermodynamic critical field $H_c(T)$. Exceeding the thermodynamic critical field $H_c(T)$ drives the type I material into the normal state. A type II superconductor also exists in the Meissner state for external fields H weaker than its lower critical field $H_{c1}(T)$, but for intermediate fields between this and its upper critical field $H_{c2}(T)$, the type II material enters the vortex state. Here the external field penetrates the sample as a lattice of flux lines, each associated with one quantum of flux Φ_0 [1] encircled by a vortex of supercurrent. The number of magnetic vortices grows linearly with the applied field H , until the superconductor becomes normal at $H = H_{c2}(T)$. Type II materials generally superconduct at much higher temperatures T and fields H than those of type I, and fully realising their technological potential requires an improved understanding of the characteristics of the vortex state.

This thesis focusses on the behaviour of the vortex core radius ρ as a function of temperature T in $\text{LuNi}_2\text{B}_2\text{C}$, as studied with muon spin rotation (μSR) spectroscopy. (For a discussion of the field dependence, see [2].) Whereas the core radius ρ is often assumed to remain constant at low temperatures $T \ll T_c$,

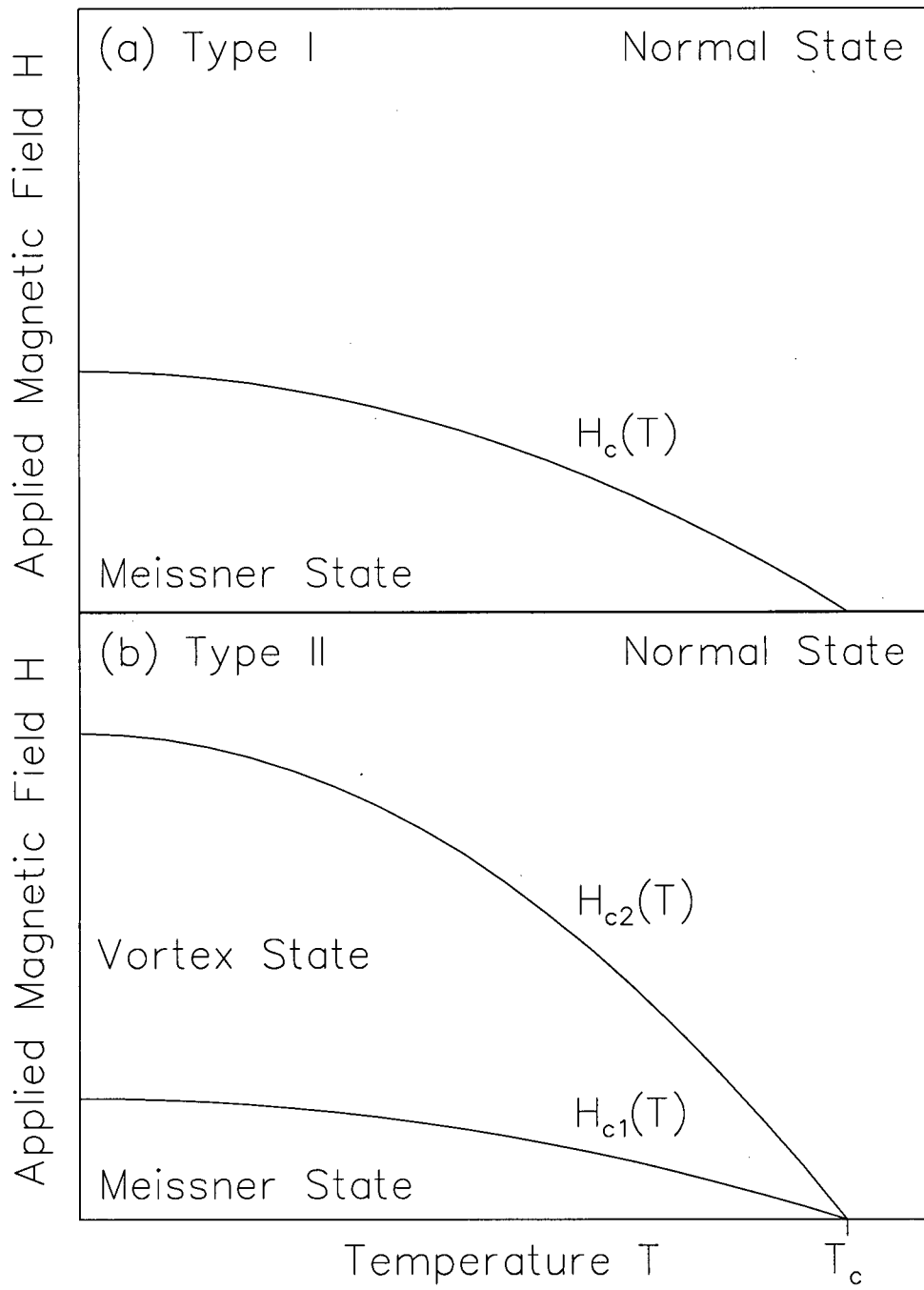


Figure 1.1: Phase diagram for (a) type I and (b) type II superconductors.

theoretical works [3][4][5] propose that the core radius ρ should contract linearly with falling temperature $T \ll T_c$, and stop shrinking at a quantum limit temperature T_0 , where the radius ρ is on the order of a Fermi wavelength. Experimental confirmation of such a temperature dependence, known as the Kramer-Pesch effect, would necessitate a reconsideration of the common assumption that the radius ρ remains constant at low temperatures. To date, μ SR observations [6][7] of the core radius ρ have revealed only a fairly weak Kramer-Pesch effect. These experiments dealt with quasi two-dimensional materials, introducing the possibility of systematic overestimation of the core radius ρ as a result of longitudinal disorder of vortices [7]. This complication has much less impact in the case of $\text{LuNi}_2\text{B}_2\text{C}$, a member of a new family of materials that exhibit unusual superconducting behaviour, because $\text{LuNi}_2\text{B}_2\text{C}$ is nearly isotropic. This superconductor is thus a prime candidate with which to see the predicted Kramer-Pesch effect.

This thesis proceeds as follows. The next chapter outlines basic relevant superconductivity concepts, and goes into detail about the expected Kramer-Pesch effect and previous experimental results concerning it. A general overview of the properties of $\text{LuNi}_2\text{B}_2\text{C}$ appears in Chapter 3, along with a quantitative estimate of the Kramer-Pesch effect anticipated for this superconductor. Chapter 4 describes the transverse field μ SR technique and the experimental setup. Chapter 5 explains how the time dependent muon polarisation signal $\mathbf{P}(t)$ is fitted to a nonlocal London model developed for borocarbides, and how the core radius ρ is calculated from the fitted internal magnetic field profile $\mathbf{B}(\mathbf{r})$. It also examines the quality of the fits as a function of the penetration depth λ , the nonlocality parameter C and the core radius ρ . Chapter 6 presents the resulting temperature dependence of the fitted penetration depth λ and nonlocality parameter C , and the extracted core radius ρ , for $\text{LuNi}_2\text{B}_2\text{C}$ under a constant applied field of $H = 1.2$ T. It compares the low temperature behaviour of the core radius ρ measured in $\text{LuNi}_2\text{B}_2\text{C}$ with the predicted Kramer-Pesch effect, as well as the core radius temperature dependences $\rho(T)$ observed previously in NbSe_2 and $\text{YBaCu}_3\text{O}_{7-\delta}$ under an applied field $H = 0.5$ T. This chapter also contrasts the internal magnetic field distributions $n(B)$ of the nonlocal and local London models. Finally, Chapter 7 summarises these results and their implications.

Chapter 2

Superconductivity

2.1 London Theory

The London equations [8] deal with the electrodynamic behaviour of superconductors on a macroscopic scale. They relate the local electric (\mathbf{E}) and magnetic (\mathbf{B}) fields to the supercurrent density \mathbf{J} as

$$\mathbf{E} = \frac{\partial}{\partial t} \left(\frac{m^*}{n_s e^2} \mathbf{J} \right) \quad (2.1)$$

$$\mathbf{B} + \lambda^2 (\nabla \times \nabla \times \mathbf{B}) = 0 \quad (2.2)$$

The supercurrent density \mathbf{J} is due to the number density n_s of carriers (either electrons or holes, depending on the superconductor) of effective mass m^* which encounter no resistance. The London penetration depth, defined as

$$\lambda = \sqrt{\frac{m^* c^2}{4\pi n_s e^2}} \quad (2.3)$$

is the only free parameter in these equations. The first London equation (2.1) expresses perfect conductivity in that the electric field accelerates the superelectrons. The second equation describes the Meissner effect. It implies that within a superconductor an external magnetic field decays over the characteristic distance λ . An example of this is the situation illustrated in Figure 2.1, where a constant applied field $B_0 \hat{\mathbf{z}}$ exists parallel to the surface at $x = 0$ of a superconductor. With the aid of the vector identity

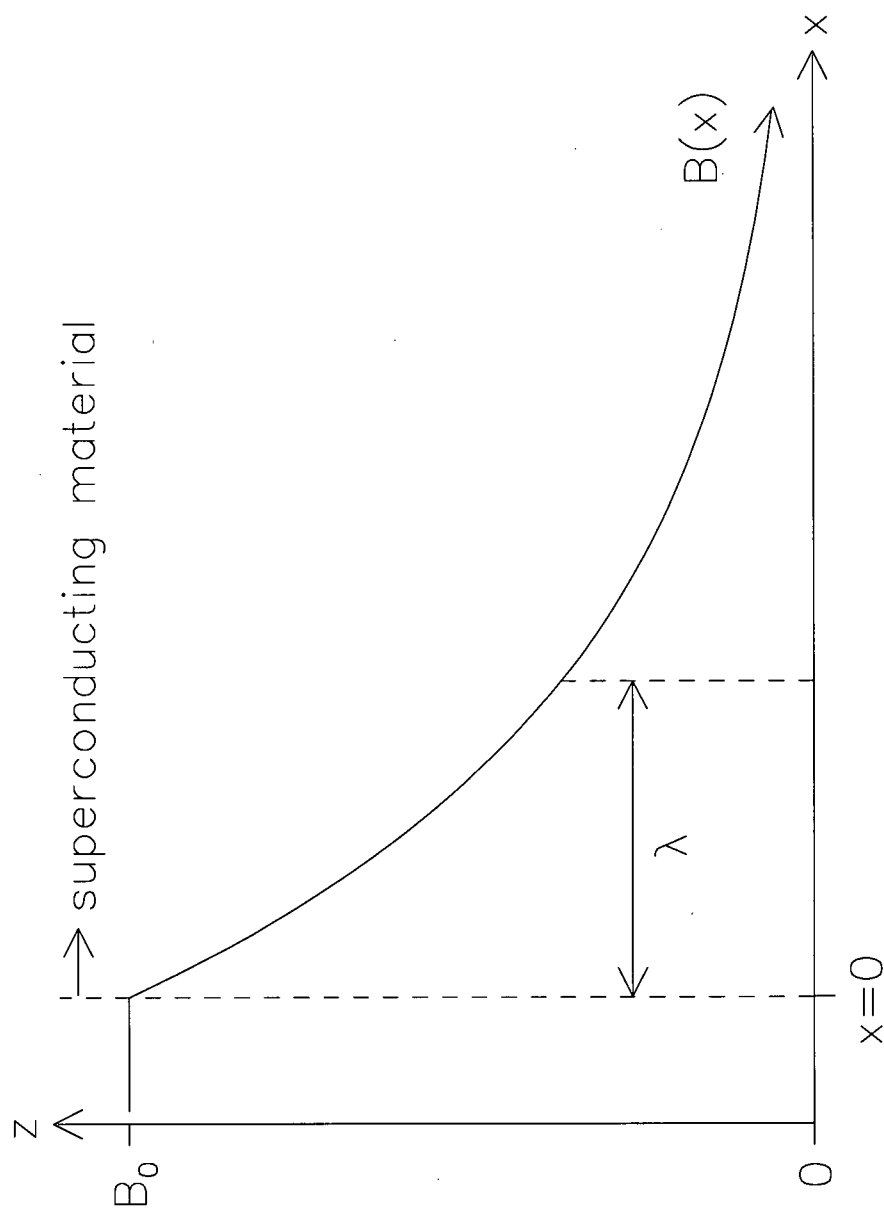


Figure 2.1: Spatial field profile $B(x) = B_0 \exp(-x/\lambda)$ below the surface at $x = 0$ of a superconductor exposed to an external field $B_0 \hat{z}$ while in the Meissner state. The penetration depth λ characterises the distance over which an applied field decays.

$$\nabla \times (\nabla \times \mathbf{a}) = \nabla (\nabla \cdot \mathbf{a}) - \nabla^2 \mathbf{a} \quad (2.4)$$

and one of Maxwell's equations, $\nabla \cdot \mathbf{B} = 0$, equation (2.2) becomes

$$B(x) = \lambda^2 \frac{\partial^2 B(x)}{\partial x^2} \quad (2.5)$$

Inside the superconductor the solution for the internal field B is then $B(x) = B_0 \exp(-x/\lambda)$, as plotted in Figure 2.1. With slight modification these London equations continue to be valid in the presence of magnetic vortices.

The spatial magnetic field profile of a vortex lattice can be modelled with a generalized London theory. For an array of flux lines at positions \mathbf{r}_i , expression (2.2) becomes [9]

$$\mathbf{B} + \lambda^2 (\nabla \times \nabla \times \mathbf{B}) = \Phi_0 \sum_i \delta_2(\mathbf{r} - \mathbf{r}_i) \quad (2.6)$$

This equation portrays each filament of one flux quantum Φ_0 as having the proportions of a two-dimensional delta function, leading to unrealistic field and supercurrent divergences at the vortex centre. Such unphysical behaviour disappears through the incorporation of finite core size, often achieved by multiplying Fourier components of the field B with a cutoff factor in reciprocal space. Equation (2.6) applies when the external field H lies far enough from the upper critical field H_{c2} that the vortices are substantially more than the radius of a physical vortex apart. The internal field then consists of the superposition of the contributions [9]

$$\mathbf{B}_i(\mathbf{r}) = \frac{\Phi_0}{2\pi\lambda^2(T)} K_0\left(\frac{|\mathbf{r} - \mathbf{r}_i|}{\lambda(T)}\right) \quad (2.7)$$

from each flux line i , where $K_0(\rho)$ is the Hankel function of imaginary argument of zero order. An explanation of the flux line lattice geometry transitions induced by external field changes in superconductors like $\text{LuNi}_2\text{B}_2\text{C}$ demands a further extension of the London equations [10][11].

Nonlocal electrodynamics accounts for the dependence of the supercurrent density $\mathbf{J}(\mathbf{r})$ on the vector potential $\mathbf{A}(\mathbf{r})$ within a characteristic range ξ_{BCS} from the point \mathbf{r} [12]. The effects of nonlocality are significant in regions where the vector potential $\mathbf{A}(\mathbf{r})$ varies rapidly within a volume of radius $\sim \xi_{BCS}$ [8][13], provided that the temperature is low and the mean free path l exceeds this radius. Otherwise scattering suppresses nonlocal effects [12]. The basic London equations (2.1) and (2.2) derive from the local relation

$$\mathbf{J}(\mathbf{r}) = -\frac{c}{4\pi\lambda^2} \mathbf{A}(\mathbf{r}) \quad (2.8)$$

by taking the time derivative and the curl respectively [8] or, in terms of spatial Fourier components [13],

$$\mathbf{J}(\mathbf{k}) = -\frac{c}{4\pi\lambda^2}\mathbf{A}(\mathbf{k}) \quad (2.9)$$

Inclusion of nonlocality transforms this equation to [12]

$$\mathbf{J}(\mathbf{k}) = -\frac{c}{4\pi\lambda^2}Q(\mathbf{k})\mathbf{A}(\mathbf{k}) \quad (2.10)$$

where the expression for the kernel $Q(\mathbf{k})$ emerges from the microscopic approach of the Bardeen-Cooper-Schrieffer (BCS) theory.

2.2 BCS Theory

BCS theory explains the occurrence of superconductivity quantum mechanically through the interaction of electrons and phonons [14][15]. One electron pulls in nearby positive ions, generating a local excess positive charge which then draws a second electron towards the first. This attraction leads to the formation of Cooper pairs. These are bound states composed of two electrons whose momenta each exceed the Fermi momentum p_F while their combined energy, both potential and kinetic, has fallen to less than $2E_F$. Although these two electrons continually scatter each other to new individual momenta, the total momentum of each Cooper pair is unchanging and identical. The net energy of a Cooper pair is lowest when it possesses zero momentum and the electrons comprising it have opposite spins. The BCS cutoff stipulates that the attraction needed to create Cooper pairs transpires only between electrons within a Debye energy $k_B\Theta_D$ of the Fermi level E_F . For this reason the number of scattering processes allowed to the electrons of a Cooper pair, and consequently the amount by which their total energy decreases, is sharply maximal when their centre of mass is stationary. The existence of more Cooper pairs leaves fewer momentum states available for scattering into, diminishing the negative potential energy associated with the attractive interaction. The BCS ground state contains as many Cooper pairs as can form with a negative potential energy of greater magnitude than the requisite kinetic energy increment. This achieves the lowest possible total energy of all the electrons. Exciting a superconductor to higher states necessitates one or more Cooper pairs breaking up.

The dissociation of a Cooper pair yields two quasiparticles [14]. These are electrons no longer restrained to occupy states of equal and opposite momenta. BCS theory

proposes that splitting up a Cooper pair needs at least an energy 2Δ . This added energy supplies the binding energy of the Cooper pair and lifts the total energy of all the electrons. Consequently no quasiparticle energy levels exist within a BCS energy gap Δ of the Fermi energy E_F . The states absent from this energy region reside at its upper bound $E_F + \Delta$, creating there a peak in the density of states $N(E)$ [16]. As the temperature T rises, the BCS energy gap $\Delta(T)$ shrinks in all k -space directions [17] and thermally excited quasiparticles become more numerous.

The BCS energy gap $\Delta(T)$ is an important superconducting parameter. A spherically symmetric gap Δ is termed s-wave pairing, while one with the symmetry of the crystal is known as anisotropic s-wave pairing. Unconventional pairing results from interactions other than that between electrons and phonons. This produces gap Δ symmetries lower than that of the crystal [16], for example an energy gap $\Delta(T)$ with nodal lines. Through the relation [18]

$$\xi_{BCS} = \frac{\hbar v_F}{\pi \Delta(0)} \quad (2.11)$$

where v_F is the Fermi velocity, the BCS energy gap Δ provides an estimate of the scale ξ_{BCS} of the spatial correlation of the superelectrons. This characteristic range ξ_{BCS} is called the BCS coherence length. The BCS energy gap Δ turns out to be directly proportional to the order parameter ψ of the Ginzburg-Landau theory.

2.3 Ginzburg-Landau Theory

The Ginzburg-Landau theory revolves around the concept of a complex order parameter $\psi(\mathbf{r})$, a pseudowavefunction describing the centre of mass motion of the Cooper pairs [1]. The distribution $|\psi(\mathbf{r})|^2$ is directly proportional to the superelectron density $n_s(\mathbf{r})$ [19]. This theory assumes local electrodynamics and is strictly valid only at temperatures near the transition temperature T_c [1]. The order parameter must be small and vary slowly to derive the Ginzburg-Landau differential equations.

The Ginzburg-Landau differential equations proceed from minimising the Helmholtz free energy f of the superconducting state [1][19]. The free energy f is expanded in powers of the order parameter $\psi(\mathbf{r})$ and its spatial derivative $\nabla\psi(\mathbf{r})$, and the effect of a magnetic field on a particle of charge e^* and mass m^* is included. Minimising the resulting free energy expression with respect to the order parameter $\psi(\mathbf{r})$ and

the internal field $B(\mathbf{r})$ gives the Ginzburg-Landau equations

$$\frac{1}{2m^*} \left(\frac{\hbar}{i} \nabla - \frac{e^*}{c} \mathbf{A}(\mathbf{r}) \right)^2 \psi(\mathbf{r}) + \beta |\psi(\mathbf{r})|^2 \psi(\mathbf{r}) = -\alpha \psi(\mathbf{r}) \quad (2.12)$$

$$\mathbf{J}(\mathbf{r}) = \frac{e^* \hbar}{i 2m^*} [\psi^*(\mathbf{r}) \nabla \psi(\mathbf{r}) - \psi(\mathbf{r}) \nabla \psi^*(\mathbf{r})] - \frac{e^{*2}}{m^* c} |\psi(\mathbf{r})|^2 \mathbf{A}(\mathbf{r}) \quad (2.13)$$

where $\mathbf{A}(\mathbf{r})$ is the vector potential associated with the internal field $\mathbf{B}(\mathbf{r}) = \nabla \times \mathbf{A}(\mathbf{r})$. The quantities α and β are expansion coefficients which depend on the penetration depth λ and the thermodynamic critical field H_c . Relations (2.12) and (2.13) form coupled differential equations for the order parameter $\psi(\mathbf{r})$ and the vector potential $\mathbf{A}(\mathbf{r})$. The first equation resembles the Schrödinger equation for a free particle plus a nonlinear term. This nonlinear term $\beta |\psi(\mathbf{r})|^2 \psi(\mathbf{r})$ encourages the order parameter $\psi(\mathbf{r})$ to spread evenly throughout space. The second equation quantum mechanically describes a current of particles of charge e^* and mass m^* . Calculations based on the microscopic BCS theory show that the effective charge e^* is twice the usual electronic charge e . Equation (2.12) also hints at another important length scale for superconductivity, the temperature dependent coherence length $\xi(T) = \hbar / \sqrt{|2m^* \alpha(T)|}$.

The temperature dependent coherence length $\xi(T)$ characterizes the distance over which changes in the order parameter $\psi(\mathbf{r})$ occur [1]. For this reason a finite coherence length $\xi(T)$ implies a gradual spatial evolution between superconducting and normal regions. Unlike the temperature independent BCS coherence length ξ_{BCS} , the Ginzburg-Landau coherence length $\xi(T)$ grows with temperature T in a manner similar to the penetration depth $\lambda(T)$.

The ratio $\kappa = \lambda(T)/\xi(T)$ of the penetration depth of a superconductor to its coherence length determines whether this material exhibits a vortex lattice. Figure 2.2 depicts the scenarios associated with the two extremes of the Ginzburg-Landau parameter κ . In both cases the order parameter ψ rises from zero to its maximum value, and the internal field \mathbf{B} drops from its maximum to zero, across the border from normal to superconducting domains. In the situation $\kappa \ll 1$ a zone exists where the field \mathbf{B} has been substantially expelled and the order parameter ψ is not yet maximal. Here the condensation energy is too small to completely compensate for the Gibbs free energy increase caused by the negative magnetisation. This leads to a positive surface energy in connection with the domain wall between the superconducting and the normal material. Conversely, in the case $\kappa \gg 1$, a boundary region arises where the positive diamagnetic energy is not enough to counteract the Gibbs free energy reduction stemming from the growing number of superelectrons. The surface energy is now negative. Calculations

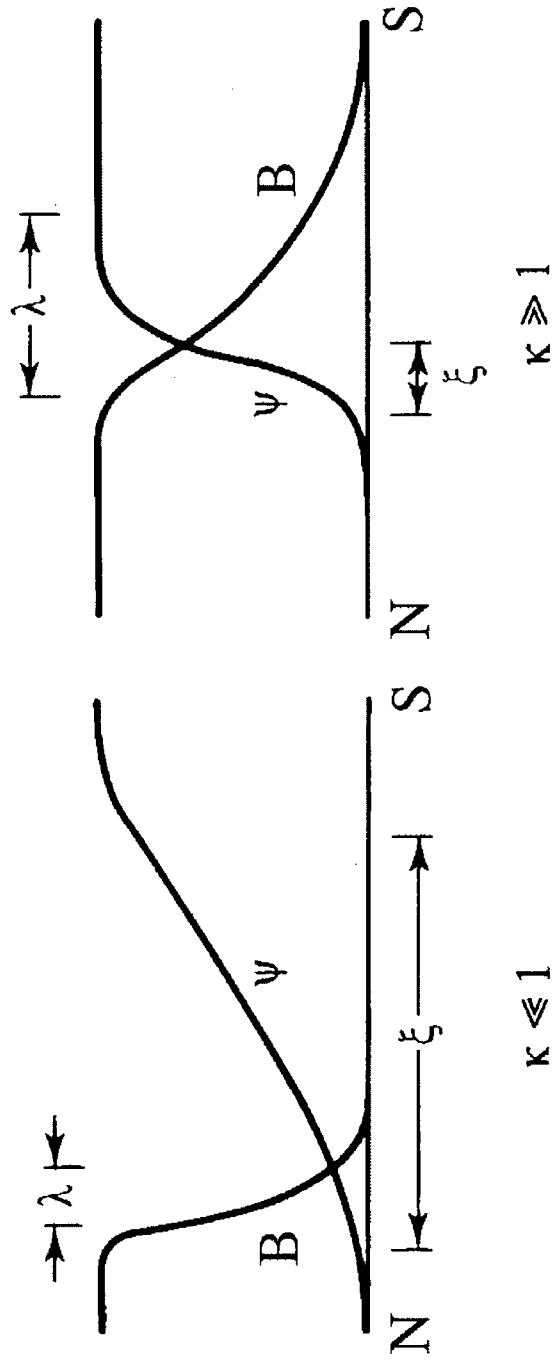


Figure 2.2: The order parameter ψ and the internal field B at the boundary between normal N and superconducting S regions for $\kappa \ll 1$ and $\kappa \gg 1$. Adapted from [1].

reveal that the surface energy of a domain wall becomes zero for a Ginzburg-Landau parameter of $\kappa = 1/\sqrt{2}$. Type I labels superconductors with a κ smaller than this, while type II refers to those with a greater κ . In type II superconductors the negative surface energy generates a regular array of flux tubes, each associated with a single flux quantum $\Phi_0 = h/2e = 2.07 \times 10^{-15} \text{ Tm}^2$. A flux line, also known as a vortex, is quasinormal at its centre, where the order parameter $\psi(\mathbf{r})$, the supercurrent density $\mathbf{J}(\mathbf{r})$ and the BCS energy gap Δ all vanish. The detailed structure of a vortex forms the subject of the next section.

2.4 The Vortex Core

In the simple view, a vortex core is a cylinder of normal material whose radius is the Ginzburg-Landau coherence length $\xi(T)$. Over this length scale the order parameter $\psi(\mathbf{r})$ and the supercurrent density $\mathbf{J}(\mathbf{r})$ fall monotonically to zero at the core centre. Although the Ginzburg-Landau formalism is only truly valid near the transition temperature T_c , the core radius is also commonly defined as the temperature dependent coherence length $\xi(T)$ at low temperatures, where it becomes approximately a BCS coherence length ξ_{BCS} [3]. Employing this assumption Caroli, de Gennes and Matricon [20] investigated the quasiparticle excitations of energy $\varepsilon \ll \Delta_\infty$ localised near an isolated vortex line in a clean ($\xi_{BCS} \ll l$) type II superconductor, where Δ_∞ is the bulk value of the BCS energy gap. They determined these quasiparticles to have at least an energy $\varepsilon_{min} \approx \Delta_\infty^2/E_F$, and above this a density of states like that of a cylindrical normal region of radius $\xi(T)$. This traditional vortex core picture implies that at low temperatures the core radius, being roughly a BCS coherence length ξ_{BCS} , is essentially temperature independent.

The Kramer-Pesch effect, predicted for isolated flux lines in clean *s*-wave superconductors [3][4][5], refers to the rapid contraction of the vortex core radius ρ to around a Fermi wavelength $1/k_F$ upon cooling at low temperatures. This flux line narrowing stems from the thermal depopulation of the quasiparticle bound states. The bound state energy levels E_μ asymptotically approach the BCS energy gap Δ_∞ as their corresponding angular momenta μ become infinite, and the low energy radial wavefunctions are greatest at a distance $r \simeq \mu/k_F$ from the core centre [4]. The reduction in core radius terminates at $\rho \sim 1/k_F$ in the quantum limit $T \lesssim T_0 = T_c/(k_F \xi_{BCS})$ [5]. Here only the lowest energy bound state remains occupied [21]. From temperature $T \ll T_c$ down to near the quantum limit

temperature T_0 , the core radius ρ shrinks linearly as

$$\rho \sim \frac{T}{T_c} \xi_{BCS} \quad (2.14)$$

Over this distance ρ away from the core centre the supercurrent density $\mathbf{J}(\mathbf{r})$ climbs to its greatest value and the pair potential $\Delta(\mathbf{r})$ rises very steeply. However the pair potential still attains its asymptotic value over a length scale comparable to the BCS coherence length ξ_{BCS} [4][21]. At the core centre the maximum internal field increases linearly as the temperature drops [22][4]. Experimental evidence for such dramatic vortex core shrinking would contradict the common assumption that, at low temperatures, the value of the core radius ρ remains constant at around a BCS coherence length ξ_{BCS} .

Experimental observations reveal the shrinking of the vortex cores upon cooling to be more limited than expected from the predicted Kramer-Pesch effect. Indirect evidence supporting the proposed Kramer-Pesch effect comes from the logarithmic singularity in the current-voltage characteristic for $\text{Nd}_{1.85}\text{Ce}_{0.15}\text{CuO}_x$ films [23]. Muon spin rotation (μSR) measurements of the core radius ρ as a function of temperature show a surprisingly weak Kramer-Pesch effect in NbSe_2 [6] ($T_c = 7.0\text{ K}$), $\text{YBaCu}_3\text{O}_{6.95}$ [7] ($T_c = 93.2\text{ K}$) and $\text{YBaCu}_3\text{O}_{6.60}$ ($T_c = 59\text{ K}$). The core radius ρ in NbSe_2 saturates at $\rho \approx 72\text{ \AA}$, many times larger than the anticipated low temperature radius ρ of around 10 \AA . The temperature dependence of the vortex size is weaker in $\text{YBaCu}_3\text{O}_{6.95}$, and even more so in $\text{YBaCu}_3\text{O}_{6.60}$. The apparent absence of significant core shrinking in $\text{YBaCu}_3\text{O}_{6.60}$ and $\text{YBaCu}_3\text{O}_{6.95}$ possibly reflects the attainment of the quantum limit [5][24][25]. The quantum limit temperature T_0 should be much higher in these materials than in NbSe_2 , since they have a considerably smaller BCS coherence length ξ_{BCS} . The substantially larger-than-predicted core radii found at very low temperatures in NbSe_2 are attributed to interactions between the vortices, and to their possible zero point motion. To date, all theoretical works concerning the Kramer-Pesch effect suppose isolated vortices, an assumption which likely fails for the transverse field μSR experiments mentioned here. Also, in quasi two-dimensional (2D) superconductors such as NbSe_2 and $\text{YBaCu}_3\text{O}_{7-\delta}$, longitudinal disorder of vortices potentially inflates the value of the core radius ρ determined with μSR , since a flux line in such materials consists of a column of 2D pancake vortices which could wobble [7]. Flux lines should be stiffer in three-dimensional (3D) superconductors, leading to a simpler dependence of the core radius ρ on temperature. This makes the clean 3D type II s -wave superconductor $\text{LuNi}_2\text{B}_2\text{C}$ an ideal candidate for observation of the predicted Kramer-Pesch effect with μSR . The next chapter describes the characteristics of this material.

Chapter 3

Material Properties of $\text{LuNi}_2\text{B}_2\text{C}$

3.1 The Nickel Borocarbide Family

The nickel borocarbides form a recently discovered class of compounds exhibiting unusual superconducting and magnetic characteristics. Their constituents combine in the ratio $\text{RNi}_2\text{B}_2\text{C}$, where R stands for a rare earth element or yttrium (Y), giving rise to the lattice shown in Figure 3.1. Each nickel atom tetrahedrally co-ordinates with the four closest borons to build Ni_2B_2 layers which alternate with RC sheets. Despite this planar composition, band structure calculations predict isotropic electronic properties [27] and resistivity measurements [28] confirm this. These materials provide an excellent opportunity to study the connection between superconductivity and magnetism.

Superconducting members of the nickel borocarbide family manifest relatively high critical temperatures T_c and mysterious field driven vortex lattice symmetry transitions. The substances are clean type II superconductors [29] with high Ginzburg-Landau parameters $\kappa \sim 5 - 15$ [30] and intermediately strong electron phonon interaction [27]. As the external magnetic field varies the vortex lattice geometry evolves from hexagonal to square, a phenomenon attributed to the squarish flux line cross section [31]. Under this transformation $\text{TmNi}_2\text{B}_2\text{C}$ ($T_c = 11.0 \text{ K}$) exhibits simultaneous transitions in magnetic order [30].

Magnetic nickel borocarbide superconductors become antiferromagnetically ordered below a Néel temperature T_N comparable to their critical temperature T_c , and have the highest Néel temperatures T_N of any superconductor [32]. $\text{ErNi}_2\text{B}_2\text{C}$

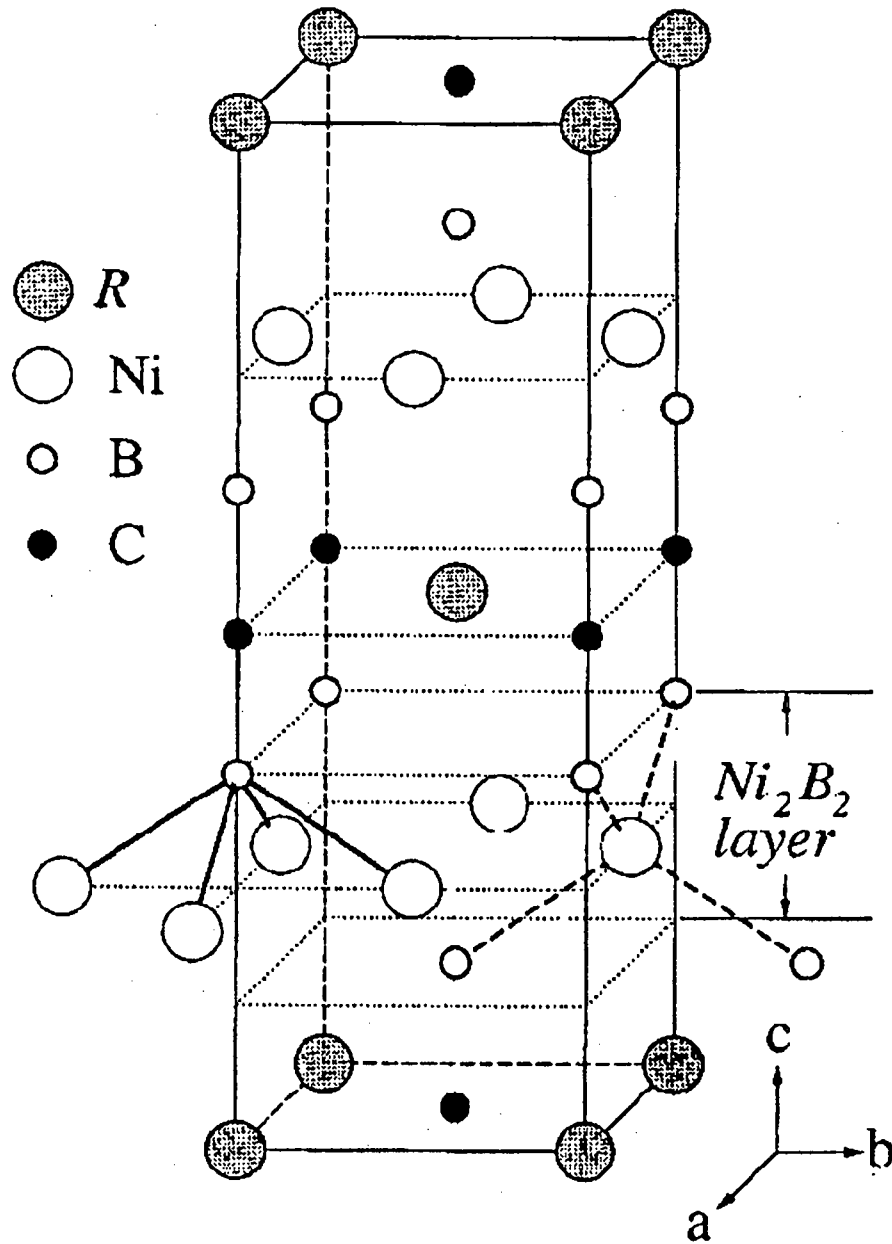


Figure 3.1: $\text{RNi}_2\text{B}_2\text{C}$ body centred tetragonal crystal structure (space group $I4/mmm$), from reference [26].

($T_c = 10.5$ K, $T_N = 6.0$ K) displays weak ferromagnetism as well when cooled below $T_{WFM} = 2.5$ K [30]. The wave vector for maximum generalised electronic susceptibility in $\text{LuNi}_2\text{B}_2\text{C}$ also characterises the incommensurate magnetic structures in superconducting $\text{ErNi}_2\text{B}_2\text{C}$ and $\text{HoNi}_2\text{B}_2\text{C}$, and in the nonsuperconductors $\text{TbNi}_2\text{B}_2\text{C}$ and $\text{GdNi}_2\text{B}_2\text{C}$ [33] [34]. A phonon mode near this wave vector softens greatly on cooling, and is comparable to the superconducting gap in energy. These observations have triggered speculation that phonon softening and magnetic ordering stem from a common Fermi surface nesting and compete to decrease the system energy. Investigation of the superconductivity of this material family, without the complications introduced by magnetism, is possible with the nonmagnetic members $\text{YNi}_2\text{B}_2\text{C}$ and $\text{LuNi}_2\text{B}_2\text{C}$.

3.2 $\text{LuNi}_2\text{B}_2\text{C}$

$\text{LuNi}_2\text{B}_2\text{C}$ has the crystal structure illustrated in Figure 3.1 with lattice parameters $a = 3.4639(1)$ Å and $c = 10.6313(4)$ Å at temperature $T = 2.3$ °C, leading to a calculated density of 8.488 g cm $^{-3}$ [35]. Table 3.1 lists the interatomic distances. The slightly shorter in-plane nickel separation, in comparison to that of metallic

Table 3.1: Interatomic distances within the $\text{LuNi}_2\text{B}_2\text{C}$ structure [35].

Atom pair	Separation (Å)
B - C	1.47
Lu - C	2.449
Lu - B	2.855
B - B	2.94
Ni - B	2.10
Ni - Ni (in Ni plane)	2.449

nickel (2.50 Å), implies a strong metallic bond. Covalent [36] B - C bonds link the LuC and Ni_2B_2 layers together. As previously mentioned, the electronic properties of $\text{LuNi}_2\text{B}_2\text{C}$ are of a strongly 3D metallic character. Band structure calculations indicate an average Fermi velocity $v_F = 2.3 \times 10^7$ cm s $^{-1}$ [37] and a sharp local maximum in the electronic density of states $N(E)$ near the Fermi surface E_F . Normal state heat capacity $C_P = C_e + C_{ph}$ measurements [38] yield a Debye temperature of $\Theta_D = 360(3)$ K, related to the phononic contribution $C_{ph} \propto T^3$, and

a Sommerfeld constant $\gamma_N = 19.5(3) \text{ mJ mol}^{-1} \text{ K}^{-2}$, the coefficient of the electronic term $C_e = \gamma_N T$. The Sommerfeld constant gives rise to an estimated Fermi surface density of states $N(E_F) = 11.8 \text{ mJ mol}^{-1} k_B^{-2} \text{ K}^{-2}$ [39]. This, together with an experimentally determined plasma energy of $\hbar\omega_{pl} = 4.0 \text{ eV}$, leads to a Fermi velocity $v_F = \sqrt{3}\hbar\omega_{pl}/[e\sqrt{4\pi N(0)}] = 2.76 \times 10^7 \text{ cm s}^{-1}$, in near agreement with band theory. In addition to these normal state properties, $\text{LuNi}_2\text{B}_2\text{C}$ also exhibits various superconducting characteristics.

The superconducting properties of $\text{LuNi}_2\text{B}_2\text{C}$ are intriguing. There exists much experimental evidence both for and against an *s*-wave pairing state [40]. Scanning tunneling microscopy [41] discloses a bulk energy gap of $\Delta = 2.2 \text{ meV}$, and thermal conductivity measurements [42] detect a large gap anisotropy $\Delta_{max}/\Delta_{min} \geq 10$. The average out of plane upper critical field anisotropy holds constant with temperature at $0.5(H_{c2}^{(100)} + H_{c2}^{(110)})/H_{c2}^{(001)} = 1.16$, as found from magnetisation studies [37]. The slight basal plane anisotropy falls from $H_{c2}^{(100)}/H_{c2}^{(110)} = 1.1$ at temperature $T = 4.5 \text{ K}$ to $H_{c2}^{(100)}/H_{c2}^{(110)} = 1.0$ by the critical temperature T_c . The initial slope of the upper critical field gives an estimated coherence length $\xi_{BCS} = 130 \text{ \AA}$. On the other hand small angle neutron scattering (SANS) [43] extracts a coherence length $\xi_{BCS} = 82(2) \text{ \AA}$ and a penetration depth $\lambda = 1060(30) \text{ \AA}$ at temperature $T = 2.2 \text{ K}$.

One of the most fascinating aspects of the superconducting behaviour of $\text{LuNi}_2\text{B}_2\text{C}$ is the occurrence of field driven transitions in its vortex lattice geometry. The evolution of the flux line lattice symmetry in $\text{LuNi}_2\text{B}_2\text{C}$, as a function of external field H , is clearly evident through Bitter decoration and SANS. Under weak fields H applied parallel to the crystal \hat{c} axis, the decoration method images a hexagonal to square vortex lattice transition [44][45]. As the magnetic field H climbs from $H = 0.002 \text{ T}$ to $H = 0.02 \text{ T}$, triangular flux line domains enlarge and one of their nearest neighbour directions becomes parallel with the $\langle 110 \rangle$ or $\langle 100 \rangle$ orientations. Raising the magnetic field H distorts the hexagonal configuration and local regions of square geometry appear above $H = 0.06 \text{ T}$. Further magnetic field increase up to $H = 0.1 \text{ T}$ reveals an expanding square proportion co-existing with a heavily distorted triangular phase. At fields H upwards of $H = 0.2 \text{ T}$, SANS records [43] a square vortex lattice which slowly becomes completely amorphous by $H = 6 \text{ T}$. SANS also shows another vortex lattice symmetry transition occurring at an external field of $\mathbf{H} = 0.3 \text{ T } \hat{\mathbf{a}}$ [46]. The hexagonal lattice reorients from having a nearest neighbour direction along the $\hat{\mathbf{b}}$ axis at lower fields H to having one along the $\hat{\mathbf{c}}$ axis at higher fields H . Whereas the geometrical transitions taking place in $\text{LuNi}_2\text{B}_2\text{C}$ for applied fields $\mathbf{H} \parallel \hat{\mathbf{c}}$ arise from nonlocal interactions, those for fields $\mathbf{H} \parallel \hat{\mathbf{a}}$ stem from energy gap Δ anisotropy [46].

The $\text{LuNi}_2\text{B}_2\text{C}$ sample examined in this μSR experiment was a single crystal 1.3 cm in diameter and 1 g in mass. The crystal grew from a mixture of Ni_2B flux and arc-melted and annealed polycrystalline $\text{LuNi}_2\text{B}_2\text{C}$ as the solution cooled from 1500°C to 1200°C over several days [47][48][33]. The sample formed as a plate, with the crystalline \hat{c} axis perpendicular to the plate plane. Thermal conductivity measurements [42] performed on this sample find an upper critical field $H_{c2}(0) \approx 7\text{ T}$. Its residual resistivity is $\rho_0 = 1.30\ \mu\Omega\text{ cm}$ and its electron mean free path is $l \approx 500\ \text{\AA}$. Resistivity data [48] from similarly grown crystals indicate that this sample should have a critical temperature $T_c = 16.0\text{ K}$.

The expected Kramer-Pesch effect for the sample studied in this experiment is that the vortex core radius ρ should contract linearly with temperature T on cooling from $T \ll 16.0\text{ K}$ ($= T_c$) down to $T \gg 0.7(1)\text{ K}$ [$= T_0$, assuming $\xi_{BCS} = 100(20)\ \text{\AA}$]. Below the quantum limit temperature $T_0 \approx 0.7\text{ K}$, the core radius ρ should stay constant at $\rho \sim 4\ \text{\AA}$ ($= 1/k_F$). The experimental setup employed to investigate this effect in $\text{LuNi}_2\text{B}_2\text{C}$ is described in the following chapter.

Chapter 4

Experiment

4.1 Transverse Field μ SR

Transverse field μ SR provides an effective means of measuring the distribution $n(B)$ of internal magnetic fields B within a superconductor. This technique employs a beam of muons polarised so that their ensemble averaged spin direction is perpendicular to their momentum, which is itself parallel to the applied field \mathbf{H} . The muons enter the sample one at a time and stop at random locations within the vortex lattice. There the spin of each muon precesses with an angular Larmor frequency $\omega = \gamma_\mu B$, directly proportional to the local magnetic field B . The magnetogyric ratio for muons is $\gamma_\mu = 851.6 \text{ Mrads}^{-1}\text{T}^{-1}$. The implanted muon decays after a mean lifetime of $\tau_\mu = 2.197 \mu\text{s}$, emitting a positron preferentially in the muon spin direction. The detection of many such positrons reveals the ensemble averaged muon spin polarisation $\mathbf{P}(t)$, also called the precession signal. The polarisation amplitude $|\mathbf{P}(t)|$ attenuates over time as the muon spins dephase due to the spatial variation of the magnetic field B within the vortex lattice. For this reason the spin precession signal $\mathbf{P}(t)$ constitutes a sensitive measure of the distribution $n(B)$ of magnetic fields B within a flux line lattice.

TRIUMF generates nearly 100% polarised muon beams through the parity violating decay of pions. The pions arise from protons, accelerated to about 500 MeV, striking a production target. Those pions decaying at rest near the target surface supply the muons employed in most modern μ SR experiments. Almost all of these positive pions (π^+) disintegrate into a positive muon (μ^+) and a muon neutrino (ν_μ)

via the weak interaction

$$\pi^+ \rightarrow \mu^+ + \nu_\mu \quad (4.1)$$

In the rest frame of these pions, the spin and momentum of neutrinos are oppositely directed. Therefore, in this frame, the spin and momentum of each muon created through process (4.1) must also be oppositely directed in order to conserve linear and angular momenta. This means that muons emitted in a given direction by pions decaying at rest are automatically highly polarised. In this way muon beams suitable for μ SR spectroscopy are produced.

The preferential emission of a positron (e^+) in the muon spin direction when a positive muon (μ^+) decays also stems from parity violation in the weak interaction. This weak decay nearly always produces an electron neutrino (ν_e) and a muon antineutrino ($\bar{\nu}_\mu$) as follows:

$$\mu^+ \rightarrow e^+ + \nu_e + \bar{\nu}_\mu \quad (4.2)$$

In the rest frame of the muon, the spin and momentum of the neutrino are antiparallel, while those of the antineutrino are parallel. When the neutrino and antineutrino are emitted in the same direction, the positron has maximum energy, and its spin direction is the same as that of the muon so as to conserve angular momentum. Consequently, the momentum of the positron reveals the spin direction of the muon at the time it decayed, since weak interactions like this one will only create a highly relativistic positron whose spin and momentum are parallel. Overall, taking into account all possible momenta of the emitted neutrino and antineutrino, the positron tends to be emitted in the muon spin direction. This enables the ensemble averaged muon spin polarisation $\mathbf{P}(t)$ to be measured.

4.2 Apparatus Setup

The experiment reported in this thesis used the M20 beamline at TRIUMF in conjunction with the Helios μ SR spectrometer to study the $\text{LuNi}_2\text{B}_2\text{C}$ sample described in Section 3.2. The M20 beamline delivers muons of mean momentum $28 \text{ MeV}/c$, so they stop throughout the bulk of the sample. Figure 4.1 illustrates the path of the muon beam through the experimental apparatus. The collimator restricts the diameter d of the muon beam to $d \approx 1 \text{ cm}$ before the beam exits the vacuum of the beamline through a thin plastic window. Each muon then triggers the muon counter (M), starting the time to digital converter (TDC). The

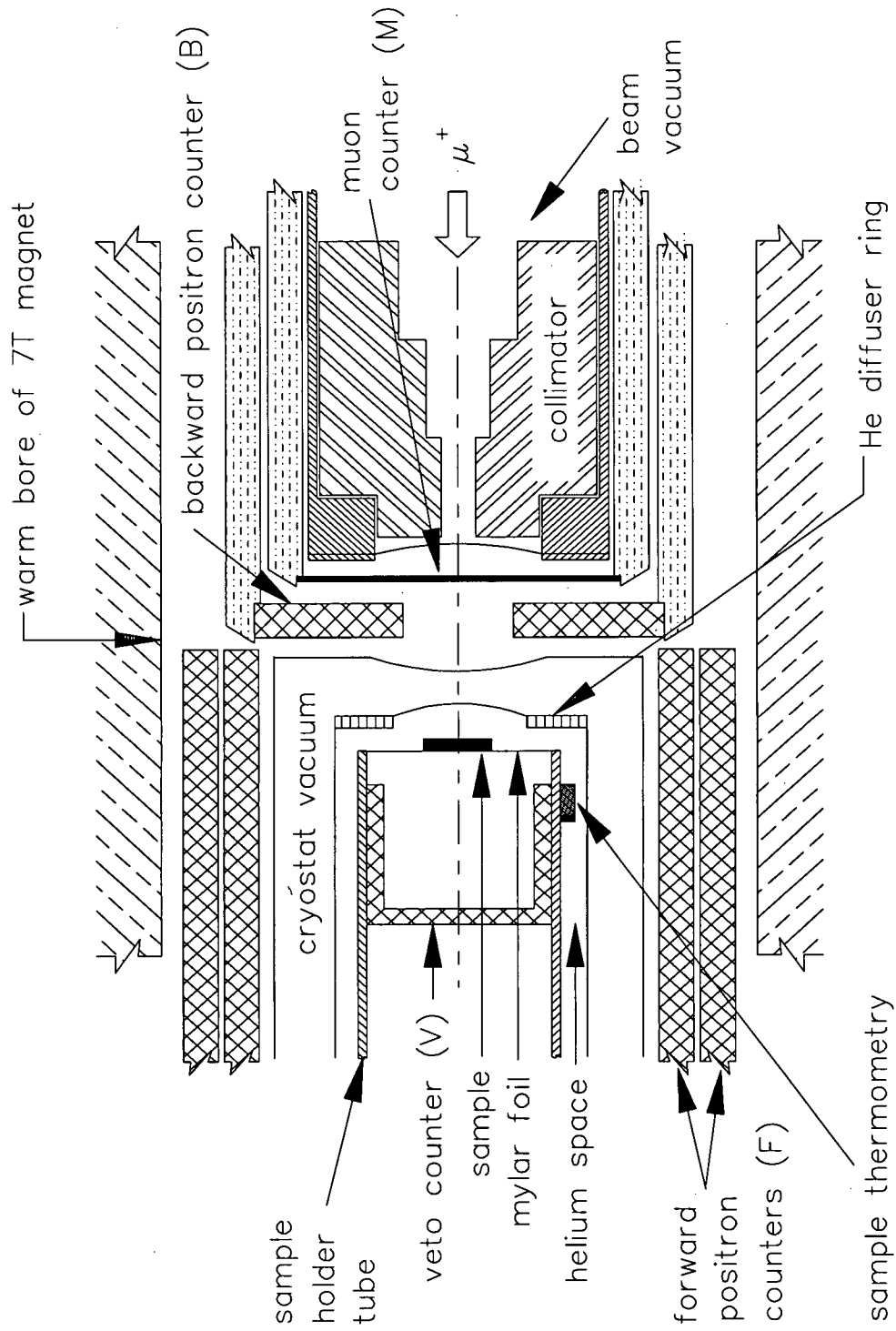


Figure 4.1: Experimental setup.

muon then travels through two more thin plastic windows, and the intervening vacuum of a helium gas flow cryostat. This vacuum thermally insulates the sample space from the warm bore of the Helios magnet. The muon finally comes to rest in the sample, which is attached with a little Apiezon N grease to a thin Mylar film stretched over the end of an aluminium sample holder tube. The crystal \hat{c} axis lies parallel to the applied field \mathbf{H} . An average of $2.197 \mu\text{s}$ later the muon decays, emitting a positron preferentially along the muon spin direction. When this positron is detected, the TDC is stopped. The TDC therefore records the elapsed time between the arrival of a muon and the detection of the subsequent decay positron. Sometimes a muon misses the sample, and instead it or its decay positron arrives at the veto (V) counter. Electronic logic modules reject such decay events, as well as ambiguous ones where the detectors register more than one muon or more than one positron within specified time periods of about $10 \mu\text{s}$.

Histograms are constructed for the number N_i of positrons detected in the i th positron counter during each time interval Δt after the TDC starts, from which the muon spin polarisation $\mathbf{P}(t)$ is computed. Figure 4.2 depicts the arrangement of the positron detectors. The positron counters form two concentric rings about the muon beam, with four counters in the inner layer and two in the outer. The inner detectors cover approximately equal solid angles around the sample, and the outer counters each completely overlap two of the inner ones. For a positron detection to be valid, both the inner and outer counters in a given direction must trigger simultaneously. The appropriate time bin of the histogram associated with that inner counter then increases by one. The number N_i of positrons registered per time bin Δt in the i th inner counter follows the form [7]

$$N_i(t) = N_i^0 \exp(-t/\tau_\mu)[1 + P_i(t)] + B_i^0 \quad (4.3)$$

where N_i^0 is a normalisation factor and B_i^0 is the random background signal. In the simple situation where all muons experience the same local field \mathbf{B} , the precession signal $P_i(t)$ recorded by the i th inner detector is $P_i(t) = A_i \cos(\gamma_\mu B t + \theta_i)$, where A_i is the initial precession amplitude and θ_i is the initial phase of the muon spin polarisation $\mathbf{P}(0)$ relative to the centre of the i th counter. Generally, these precession signals $P_i(t)$ are extracted numerically from equation (4.3). The single-counter functions $P_i(t)$ belonging to each pair of opposing inner detectors combine to produce a component of the complex muon spin polarisation $\tilde{P}(t) = P_x(t) + iP_y(t)$. Half the difference of the single-counter functions $P_i(t)$ of an opposing pair constitutes a polarisation component $P_x(t)$ or $P_y(t)$, depending on the choice of detector pair. The complex polarisation $\tilde{P}(t)$ so obtained is then fitted to a theoretical model to extract the superconducting parameters of interest. In the experiment reported in this thesis, the four histograms $N_i(t)$ together typically

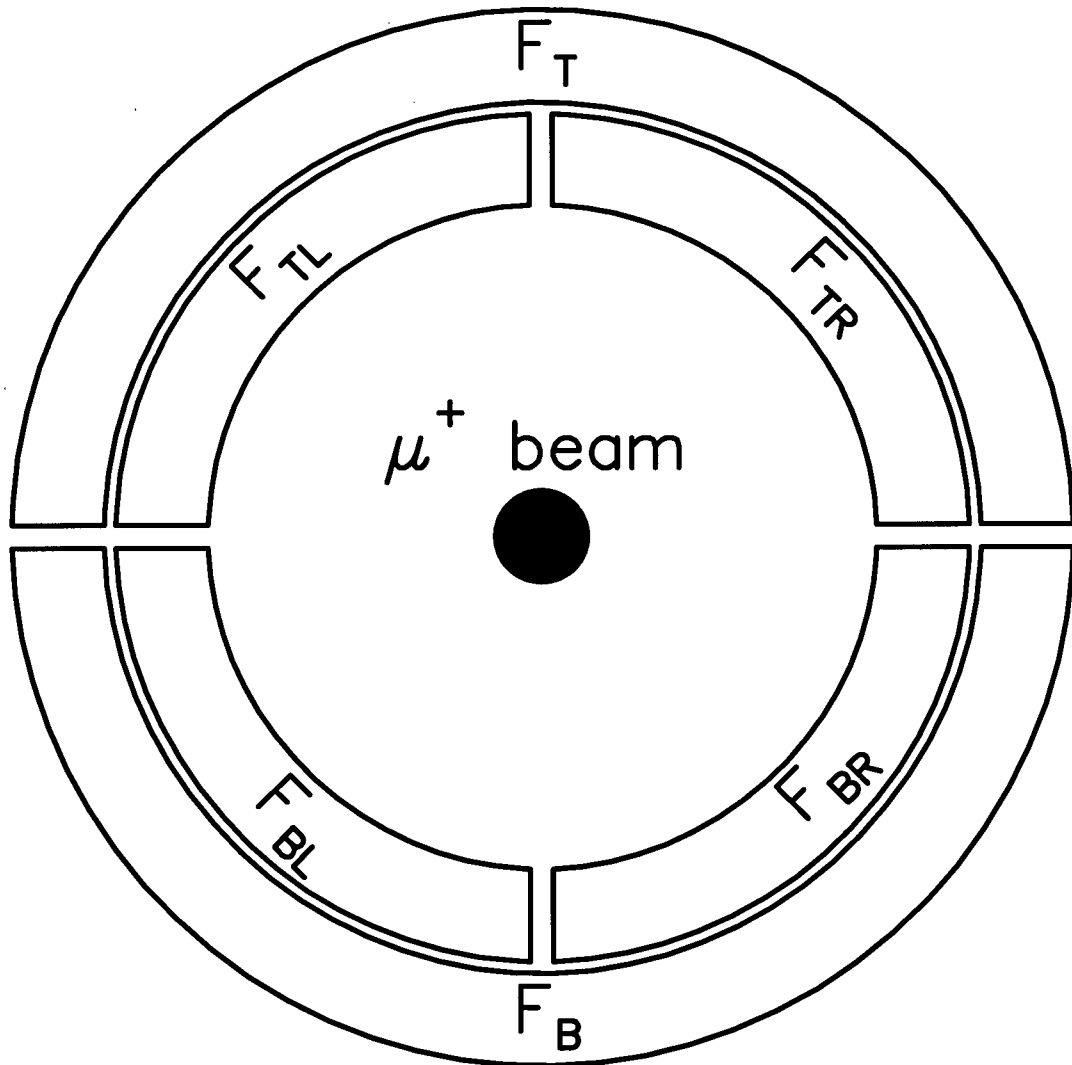


Figure 4.2: Cross-sectional view of forward positron counters F_i and F_{ij} ($i = T$ or B and $j = L$ or R) as seen by the muon beam (represented as travelling into the page). The valid detection of a decay positron requires both the F_i and F_{ij} counters to trigger simultaneously ($F_i \cdot F_{ij}$).

contained around 2.7×10^7 decay events for a given applied magnetic field H and temperature T , which were gathered over about two hours.

Feedback control systems stabilise the applied field H and temperature T . Current carrying copper coils on the outside of the Helios superconducting magnet compensate for field drifts detected with a Hall probe situated near the sample. This keeps external field H fluctuations below 0.05 mT. Helium streaming past the sample from the nearby diffuser supplies cooling power, while a Lakeshore 330 autotuning temperature controller heats the diffuser. The heating varies in such a way as to maintain the temperature of the diffuser at the set value. One calibrated GaAlAs diode monitors the diffuser temperature, and two others provide independent readings of the sample temperature. The analysis of the collected data is explained in the next chapter.

Chapter 5

Analysis

5.1 Data Fitting in the Time Domain

The μ SR data are fitted to a theoretical model of the magnetic field B within a type II superconductor. The approximate field distribution $n(B)$ yielded by taking the real amplitude of the Fourier transform of the measured muon spin polarisation $\tilde{P}(t)$ is not useful for fitting, since the inherent finite time window introduces distortions in the form of ringing and broadening. To avoid these problems, all the results reported in this thesis come from fits in the time domain.

Fitting the recorded muon polarisation to a function calculated from a theoretical field B model forms the basis of a time domain analysis. The polarisation function

$$\begin{aligned} \tilde{P}(t) = A \exp(-\sigma_d^2 t^2 / 2) \int_{-\infty}^{\infty} n(f) \exp[i(2\pi f t + \theta)] df \\ + A_b \exp(-\sigma_b^2 t^2 / 2) \exp[i(2\pi f_b t + \theta_b)] \end{aligned} \quad (5.1)$$

utilised to fit the μ SR data consists of a contribution from the muons that land in the superconducting sample and a term describing the background signal created by those that miss it. The parameters A and A_b reflect respectively the initial amplitudes of the superconducting and background asymmetries, or spin polarisations. The Gaussian damping factors $\exp(-\sigma_d^2 t^2 / 2)$ and $\exp(-\sigma_b^2 t^2 / 2)$ model the field B inhomogeneity which is additional to that of a regular array of vortices [49]. In the case of the superconducting signal the main sources of this are nuclear dipolar fields and vortex lattice disorder. The phase angles θ and θ_b account

for the amount of spin precession that occurs *before* the muons trigger the muon counter. The vortex lattice field model described in the next section determines the distribution $n(f)$ of Larmor precession frequencies f .

5.2 Model for the Internal Field Distribution

The μ SR data is fitted to a London model [11] that incorporates the effects of nonlocality through a kernel $Q(\mathbf{k})$, an extension described in Section 2.1. As mentioned in that section, the London model is inapplicable within a vortex core. Despite this the theory can yield the vortex lattice structure belonging to high κ superconductors, such as $\text{LuNi}_2\text{B}_2\text{C}$, under weak external fields $H \ll H_{c2}$, because in these situations the intervortex spacing greatly surpasses the diameter of a core [10]. $\text{LuNi}_2\text{B}_2\text{C}$ exhibits both square and triangular vortex structures according to the field \mathbf{H} applied, as discussed in Chapter 3. This nonlocal theory is chosen to fit the μ SR data since it accounts for an observed vortex lattice transformation between these two geometries in $\text{LuNi}_2\text{B}_2\text{C}$, and because the data are collected under low field ($H \ll H_{c2}$) conditions.

Expanding [11] the BCS kernel $Q(\mathbf{k})$, for weak currents \mathbf{J} , to first order in the small term $k^2\xi_{BCS}^2$ leads to the internal spatial field profile $\mathbf{B}(\mathbf{r})$ of a nonlocal London model:

$$\mathbf{B}(\mathbf{r}) = \hat{\mathbf{z}}\bar{B} \sum_{\mathbf{k}} \frac{\exp(i\mathbf{k} \cdot \mathbf{r}) \exp(-k^2\xi^2/2)}{1 + \lambda^2k^2 + \lambda^4C(0.0705k^4 + 0.675k_x^2k_y^2)} \quad (5.2)$$

where the co-ordinates (x, y, z) coincide with the crystal frame (a, b, c) and the external field \mathbf{H} is in the $\hat{\mathbf{z}}$ direction. The average magnetic field inside the superconducting sample is \bar{B} . The constant co-efficients 0.0705 and 0.675 arise from the evaluation of Fermi surface averages of products of Fermi velocities according to $\text{LuNi}_2\text{B}_2\text{C}$ band structure. The Gaussian cutoff factor $\exp(-k^2\xi^2/2)$ in the sum over the reciprocal lattice vectors \mathbf{k} of the vortex lattice compensates for the failure of the London approach within the core region. This model neglects vortex-vortex interactions. The parameter C reflects the strength of the nonlocal effects, and contains several poorly known factors.

The nonlocality parameter C varies theoretically with temperature T as [11]

$$C(T) \propto \left(\frac{\rho_{nl}(T)}{\lambda(T)} \right)^2 \quad (5.3)$$

where $\rho_{nl}(T)$ is the nonlocality radius, on the order of the BCS coherence length ξ_{BCS} [12]. Figure 5.1 shows the numerically calculated behaviour of the penetration depth $\lambda(T)$, the nonlocality radius $\rho_{nl}(T)$ and the nonlocality parameter $C(T)$ as functions of temperature. The relation [12]

$$\frac{1}{\lambda^2(T)} \propto T \Delta^2(T) \sum_{\hbar\omega(T) > 0} \{\Delta^2(T) + [\hbar\omega(T)]^2\}^{-3/2} \quad (5.4)$$

where $\hbar\omega(T) = \pi k_B T (2n + 1)$ are the Matsubara frequencies and n is a non-negative integer, gives the expected temperature dependence of the penetration depth λ in the clean limit. Solving [13] the equation

$$\frac{1}{N(0)V} = \int_0^{k_B \Theta_D} \frac{\tanh \left[\frac{1}{2k_B T} \sqrt{\xi^2 + \Delta^2(T)} \right]}{\sqrt{\xi^2 + \Delta^2(T)}} d\xi \quad (5.5)$$

determines the BCS energy gap $\Delta(T)$, where $k_B \Theta_D$ is the Debye energy, $N(0)$ is the density of states at the Fermi level for electrons of one spin orientation, and V describes the strength of the interaction potential for scattering a Cooper pair. Evaluating the above integral at temperature $T = T_c$ reveals the constant $N(0)V$ to be

$$\frac{1}{N(0)V} = \gamma + \ln \left(\frac{2\Theta_D}{\pi T_c} \right) \quad (5.6)$$

where $\gamma = 0.5772 \dots$ is Euler's constant. The calculations plotted in Figure 5.1 assume a critical temperature $T_c = 16$ K and a Debye temperature $\Theta_D = 360$ K, values appropriate for $\text{LuNi}_2\text{B}_2\text{C}$. The expression [12]

$$\rho_{nl}^2(T) \propto \frac{\sum_{\hbar\omega(T) > 0} \{\Delta^2(T) + [\hbar\omega(T)]^2\}^{-5/2}}{\sum_{\hbar\omega(T) > 0} \{\Delta^2(T) + [\hbar\omega(T)]^2\}^{-3/2}} \quad (5.7)$$

generates the clean limit behaviour of the nonlocality radius $\rho_{nl}(T)$ shown in this figure. The above sums over $\hbar\omega(T)$ converge by $\hbar\omega(T) \approx 2k_B \Theta_D$. Combining the temperature dependence of the penetration depth $\lambda(T)$ and the nonlocality radius $\rho_{nl}(T)$ according to (5.3) produces the temperature variation of the internal field model parameter C , displayed in Figure 5.1. The next section describes the software utilised to fit this internal field model to the experimental data.

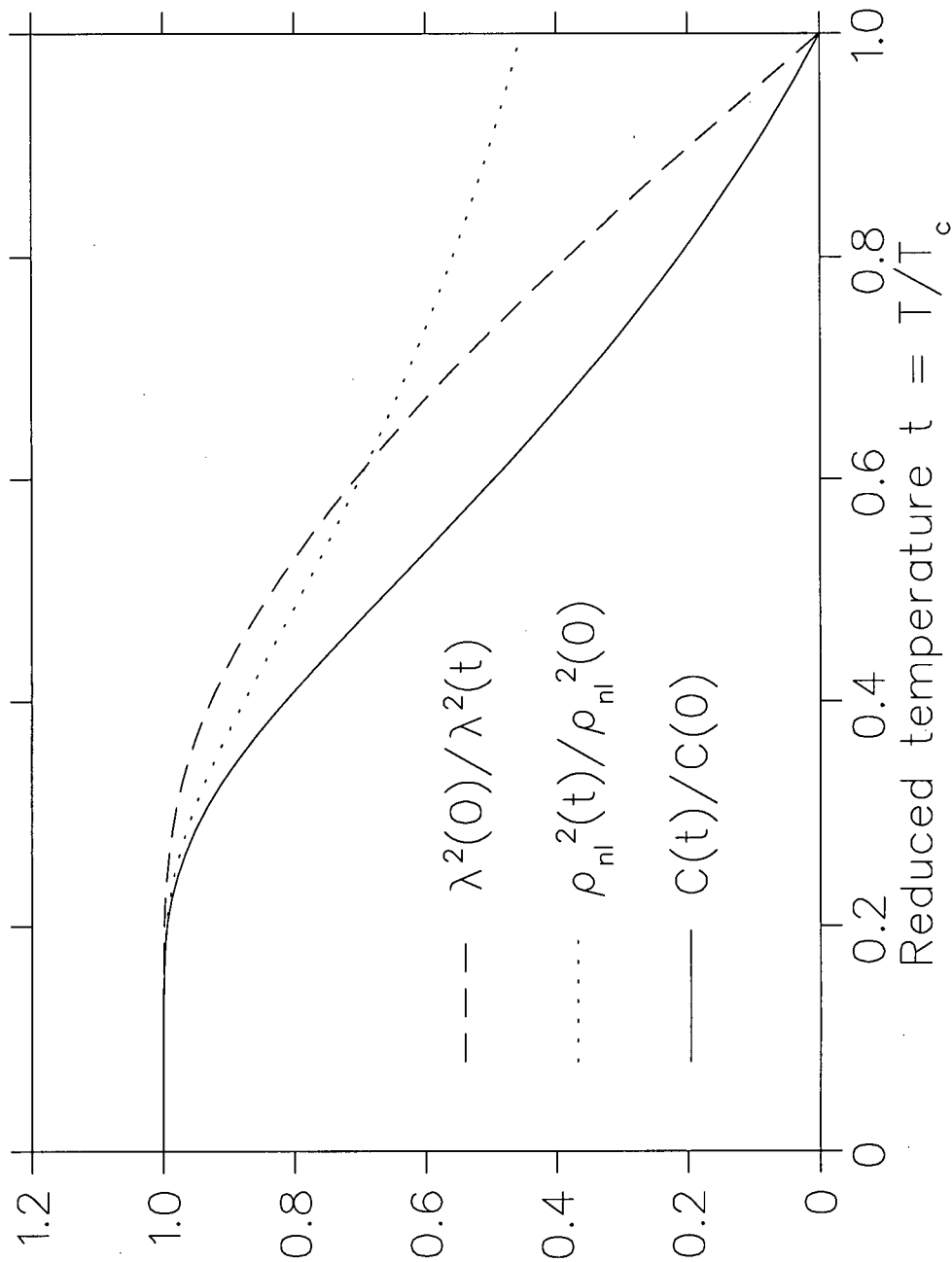


Figure 5.1: Expected temperature T dependence of parameter C , as computed from the penetration depth $\lambda(T)$ and the nonlocality radius $\rho_{nl}(T)$ in the clean limit.

5.3 Fitting Software

The computer code for fitting the internal field model to the measured muon spin polarisation $\tilde{P}(t)$ is written in FORTRAN. The software incorporates Minit function minimisation and error analysis routines from the European Organisation for Nuclear Research (CERN) program library. Using trial parameter values, the fitting program calculates the distribution $n(f)$ of muon precession frequencies f according to the field model, and then from $n(f)$ evaluates the corresponding polarisation function (5.1). The code then computes the chi-squared χ^2 between this function and the experimentally recorded muon spin polarisation $\tilde{P}(t)$. Minit selects new trial values for the variable parameters until it minimises χ^2 . The fitting program evolved from an earlier version [49] to include the nonlocal corrections outlined in the previous section and a square vortex lattice geometry.

The fitting program determines the model distribution $n(f)$ of muon frequencies f by sampling the internal field B on a grid of evenly spaced points within the vortex lattice primitive cell. Previous observations (see Chapter 3) indicate that $\text{LuNi}_2\text{B}_2\text{C}$ has a square vortex lattice at the applied field $H = 1.2\text{ T}$ of the data analysed in this thesis. Therefore the muon frequency distribution $n(f)$ calculation employs the vortex and reciprocal lattice vector geometry appropriate to a square lattice under an applied field \mathbf{H} aligned with the crystalline \mathbf{c} axis. In this case the vortex lattice primitive axes \mathbf{b}_1 and \mathbf{b}_2 are

$$\mathbf{b}_1 = \frac{b}{\sqrt{2}}(\hat{\mathbf{x}} + \hat{\mathbf{y}}) \quad (5.8)$$

$$\mathbf{b}_2 = \frac{b}{\sqrt{2}}(-\hat{\mathbf{x}} + \hat{\mathbf{y}}) \quad (5.9)$$

where the intervortex spacing $b = \sqrt{\Phi_0/B}$. Figure 5.2 shows the sampled locations inside the vortex lattice unit cell. The square symmetry of the vortex lattice means the fitting software only needs to sample one eighth of the unit cell. Then, when evaluating the polarisation (5.1), the program weights contributions from locations on the edge of the sampled area by a compensatory factor of one half. Similar symmetry considerations in reciprocal space greatly shorten the time required to compute the field (5.2), and hence dramatically speed up the fitting process. The analysis utilises a sampling density of 5184 points per vortex lattice primitive cell. This density is sufficient since halving it only produces small changes ($< 0.001\%$) in the best-fit values of the penetration depth λ and the nonlocality parameter C , and in the calculated core radius ρ .

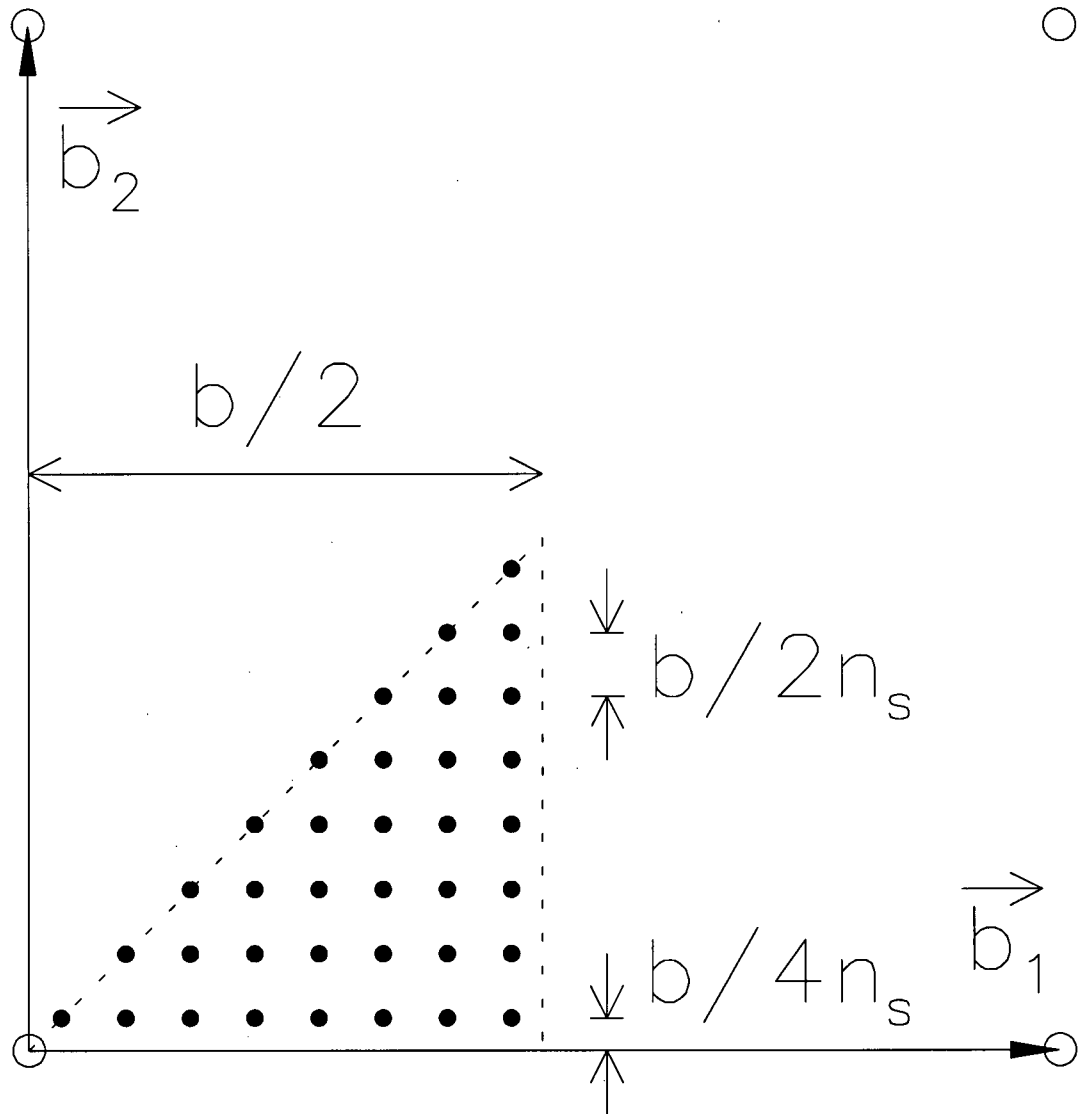


Figure 5.2: Geometry for $n_s^2/2 = 32$ sampling points within one eighth of the vortex lattice unit cell. The dashed line and the b_1 axis bound the sampled region. The closed circles depict sampling points while the open ones symbolise vortices. For data analyses $n_s^2/2 = 648$.

The ten fitted parameters are

- the average muon precession frequency of the superconducting signal $\bar{f} = \gamma_\mu \bar{B} / 2\pi$,
- the penetration depth λ ,
- the nonlocality parameter C ,
- the effective coherence length ξ ,
- the initial amplitude of the asymmetry of the superconducting signal A ,
- the initial phase angle of the superconducting signal θ ,
- the effective depolarisation rate of the the superconducting signal σ_d due to nuclear dipoles and vortex lattice disorder,
- the average muon precession frequency of the background signal f_b ,
- the initial phase angle of the background signal θ_b , and
- the effective depolarisation rate of the background signal σ_b .

The data fitting proceeds by alternately letting only the superconducting and then only the background signal parameters vary, until all the variables converge to the final result. Allowing the initial phases θ and θ_b of the superconducting and background signals to vary separately significantly improves fit quality. During early fitting attempts the initial background asymmetry A_b also varied and grew unphysically large. Therefore throughout all subsequent fits the initial background asymmetry A_b is fixed to 0.0044, as estimated by comparing fast Fourier transforms (FFT) of the polarisation signals measured in the superconducting and normal states. In comparison, the asymmetry A of the superconducting signal is much greater at $A = 0.237(2)$. The fitting takes place within a rotating reference frame set to the expected background signal frequency f_b , facilitating easy visual inspection of the accuracy of a fit. Knowledge of the best-fit values for the internal field model parameters enables the extraction of the vortex core radius ρ .

5.4 Calculation of the Core Radius

Substituting the fitted parameters into expression (5.2) reveals the spatial profile of the internal field $\mathbf{B}(\mathbf{r})$ within the sample. Figure 5.3 displays the profile around a flux line generated by an external field $H = 1.2$ T at temperature $T = 2.6$ K. The inset contains the internal field distribution $n(B)$ belonging to this spatial profile and, for comparison, the real amplitude of the FFT of the recorded precession signal $\tilde{P}(t)$. The two distributions are similar; however, as alluded to in Section 5.1, the finite time span of the μ SR data broadens the FFT and creates rapid oscillations in it. This ringing is especially visible in the high field B tail of the FFT, despite the FFT having undergone apodisation to smooth it. Apodisation effectively convolutes the FFT with a Gaussian function, and so broadens the distribution still further. Nuclear dipolar fields and slight vortex lattice disorder also broaden this distribution. The small peak in the FFT at field $B \approx 1.204$ T arises from muons that miss the sample. The maximum peak in the FFT, and in the fitted field distribution $n(B)$, occurs for the field B located at the midpoint between nearest neighbour vortices. The shoulder corresponding to fields B weaker than this, expected for a square vortex lattice according to the local London model, is absent here in both the fitted field distribution $n(B)$ and the FFT of the recorded polarisation $\tilde{P}(t)$. This lack of a sizeable low field shoulder is a consequence of nonlocality. The effect of nonlocality on the field distribution $n(B)$ appears in more detail in the next chapter. The very high fields B in the field distribution $n(B)$ of a flux line lattice derive from the vortex core region.

A useful definition of the radius ρ of a vortex core is the distance r from the core centre to the point where the supercurrent density $J(r)$ is greatest. Applying one of Maxwell's equations,

$$\mathbf{J}(\mathbf{r}) = \nabla \times \frac{1}{\mu} \mathbf{B}(\mathbf{r}) \quad (5.10)$$

where the constant μ is the permeability of the medium, to the fitted internal field $\mathbf{B}(\mathbf{r})$ readily supplies the supercurrent density $\mathbf{J}(\mathbf{r})$. Figure 5.4 depicts the computed supercurrent density $J(r)$ along a straight line between nearest neighbour vortices, and the extracted core radius ρ , due to an external field $H = 1.2$ T at temperature $T = 2.6$ K. The supercurrent density $J(r)$ grows from zero at the vortex centre to its maximum value at the core radius ρ , and then subsides until it vanishes at the midpoint between adjacent vortices. All core radius values presented in this thesis are deduced from the fitted field $\mathbf{B}(\mathbf{r})$ in this way. Core radii determined by these means are relatively insensitive, compared to the fitted

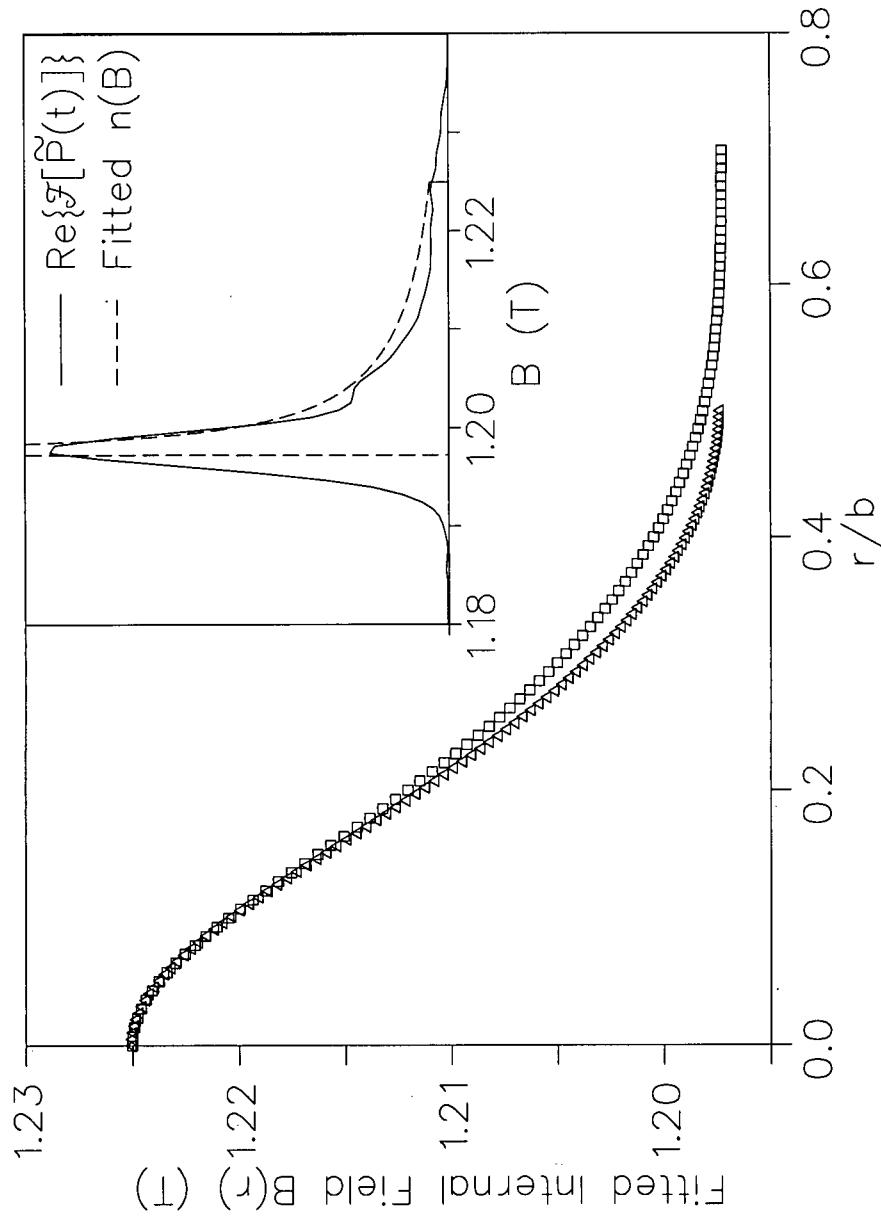


Figure 5.3: Fitted internal field $B(\mathbf{r})$ in $\text{LuNi}_2\text{B}_2\text{C}$ at temperature $T = 2.6 \text{ K}$ in an applied field $H = 1.2 \text{ T}$. The spatial profiles are along a diagonal (squares) and an edge (triangles) of the unit cell with vortices at each corner. The distance r from a vortex is given relative to the nearest neighbour vortex separation $b = 415 \text{ \AA}$. Inset: Fitted internal field distribution $n(B)$ (dashed curve), and real amplitude (solid curve) of the FFT \mathcal{F} of the measured muon spin polarisation $\tilde{P}(t)$.

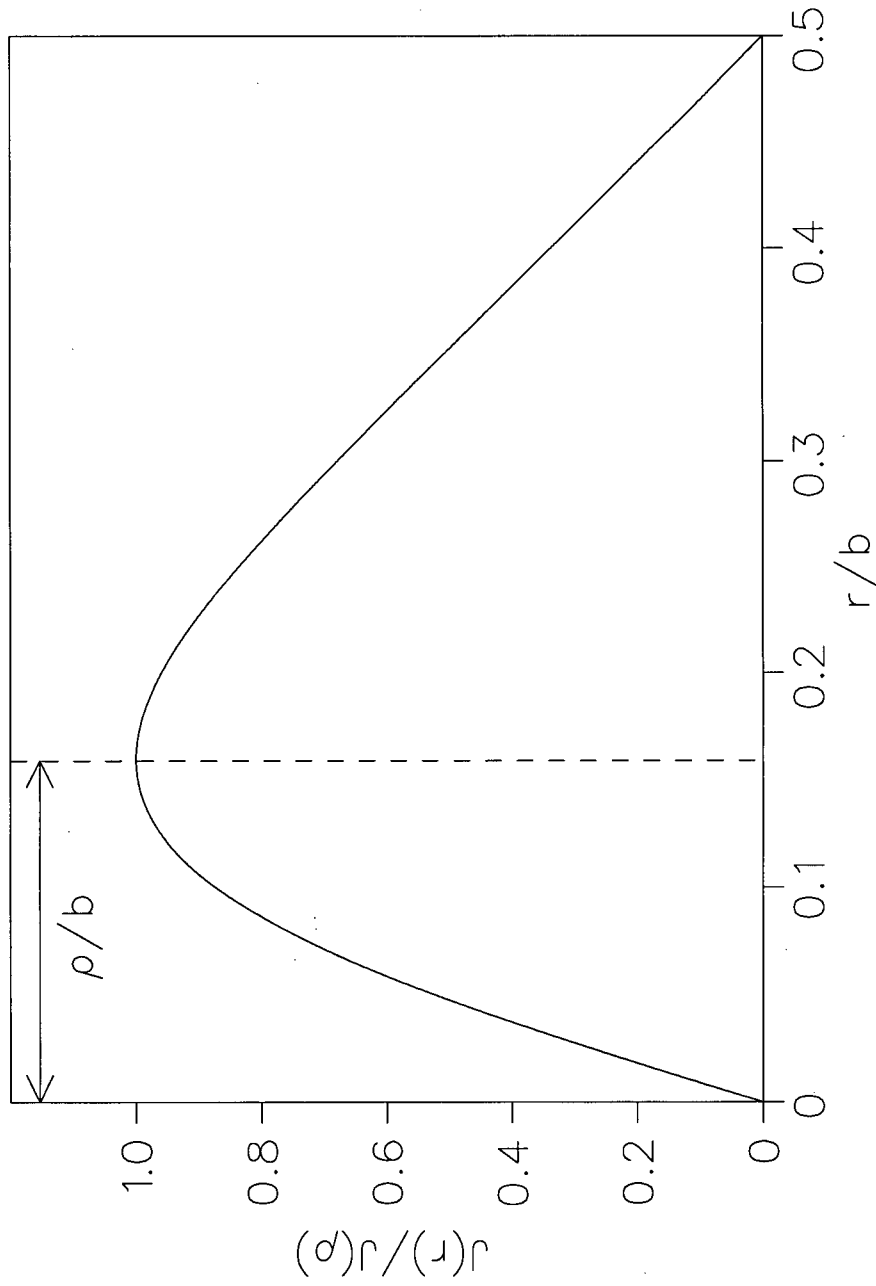


Figure 5.4: Calculated supercurrent density $J(r)$ along a line connecting adjacent vortices, and consequent vortex core radius ρ , for $\text{LuNi}_2\text{B}_2\text{C}$ at temperature $T = 2.6 \text{ K}$ and applied field $H = 1.2 \text{ T}$. The distance r from a vortex centre is indicated relative to the nearest neighbour intervortex spacing $b = 415 \text{ \AA}$.

parameters, to the specific choice of internal field model, as long as the model reproduces the actual field of the vortex lattice reasonably well [7]. This is because the calculated supercurrent density $J(r)$, and hence the core radius ρ , depend only on the spatial profile of the internal field $B(\mathbf{r})$. The accuracy to which the model reconstructs the field $B(\mathbf{r})$ can be inferred from the quality of the fit between the measured muon precession signal $\tilde{P}(t)$ and that predicted by the model.

5.5 Fit Quality

Figure 5.5 displays a typical fitted muon precession signal $\tilde{P}(t)$ in a rotating reference frame. The fitted function passes through most of the data points. The insets to this figure contain residual plots which exhibit a clear oscillation, indicating that the fitted function describes the data imperfectly. Such plots offer a useful qualitative assessment of the accuracy of a fit.

Chi-squared χ^2 provides a quantitative evaluation of the fit quality. It is defined as

$$\chi^2 = \sum_{i=1}^n \frac{(f(x_i) - y_i)^2}{(\delta y_i)^2} \quad (5.11)$$

where $f(x)$ is the function fitted to the n measurements $y_i \pm \delta y_i$. A decrease in χ^2 of at least one reveals a significantly improved fit, while a reduced chi-squared $\chi^2/n \leq 1$ means the fit is perfect. For the results reported in this thesis, the minimised reduced chi-squareds range between $\chi^2/n = 1.53$ and $\chi^2/n = 1.84$. These fits are comparable in quality to those obtained for other superconductors through analysis of μ SR data in the time domain. Use of a more accurate cutoff factor [50] than the simple Gaussian $\exp(-k^2\xi^2/2)$ in expression (5.2) might supply better fits for the $\text{LuNi}_2\text{B}_2\text{C}$ data discussed in this thesis. Figure 5.6 shows the dependence of χ^2/n on the penetration depth λ in $\text{LuNi}_2\text{B}_2\text{C}$ at several temperatures T , and Table 5.1 lists the number of degrees of freedom n for each of these temperatures. (The number of degrees of freedom n for fits at other temperatures is similar.) For each set value of the penetration depth λ the parameters vary, in the way described in Section 5.3, until χ^2 is minimised. The error bars for fitted parameters reported in this thesis are the amount by which the parameter must change to raise χ^2 by one while the other parameters vary normally. At each temperature there is a clear minimum in χ^2/n as a function of penetration depth λ , which moves to higher values of the penetration depth λ at warmer temperatures. The shallowness of the minima is at least partly a consequence of compensation by the other free

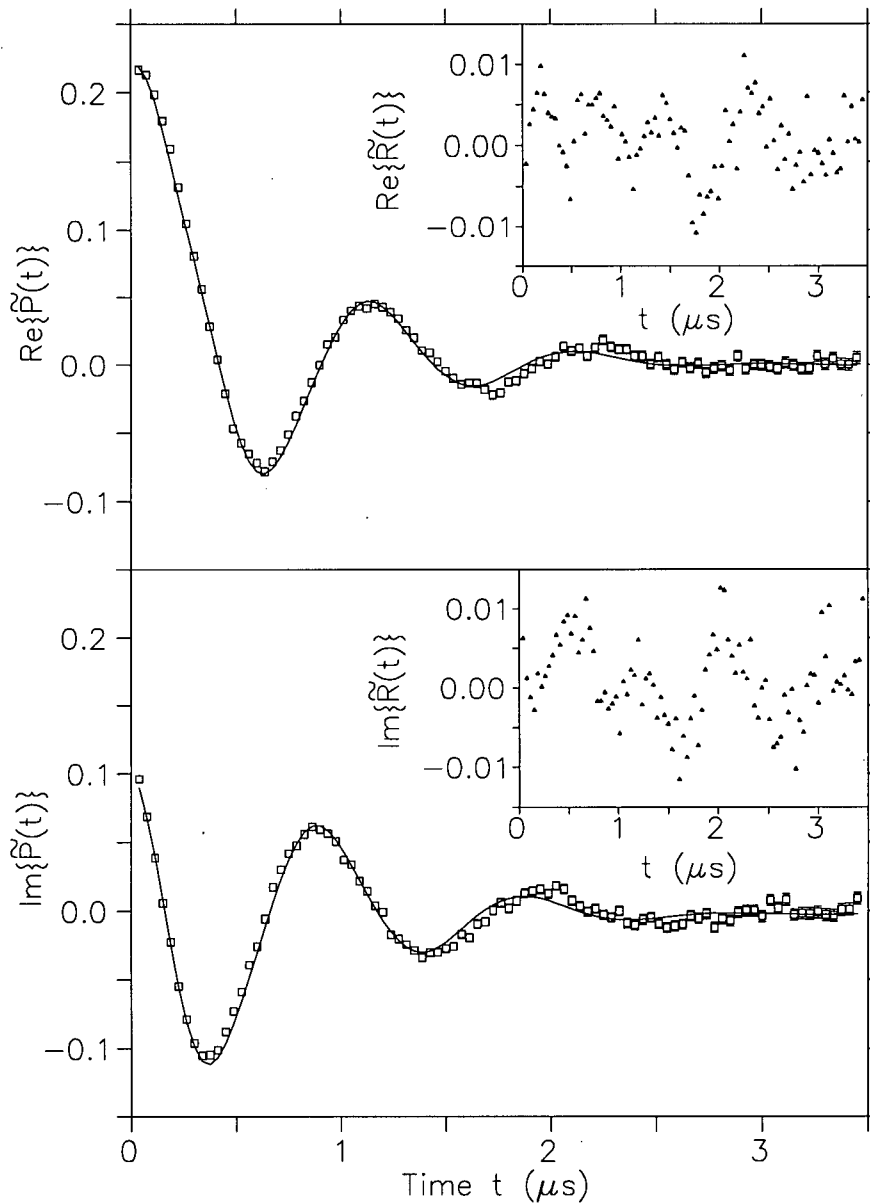


Figure 5.5: Fitted muon polarisation $\tilde{P}(t)$ in $\text{LuNi}_2\text{B}_2\text{C}$ under an applied field $H = 1.2\text{ T}$ at temperature $T = 2.6\text{ K}$. The real and imaginary polarisation components are perpendicular to the field. The squares represent data while the solid lines are the fitted function (5.1). The insets show the residuals $\tilde{R}(t)$ formed by subtracting the fitted function from the data.

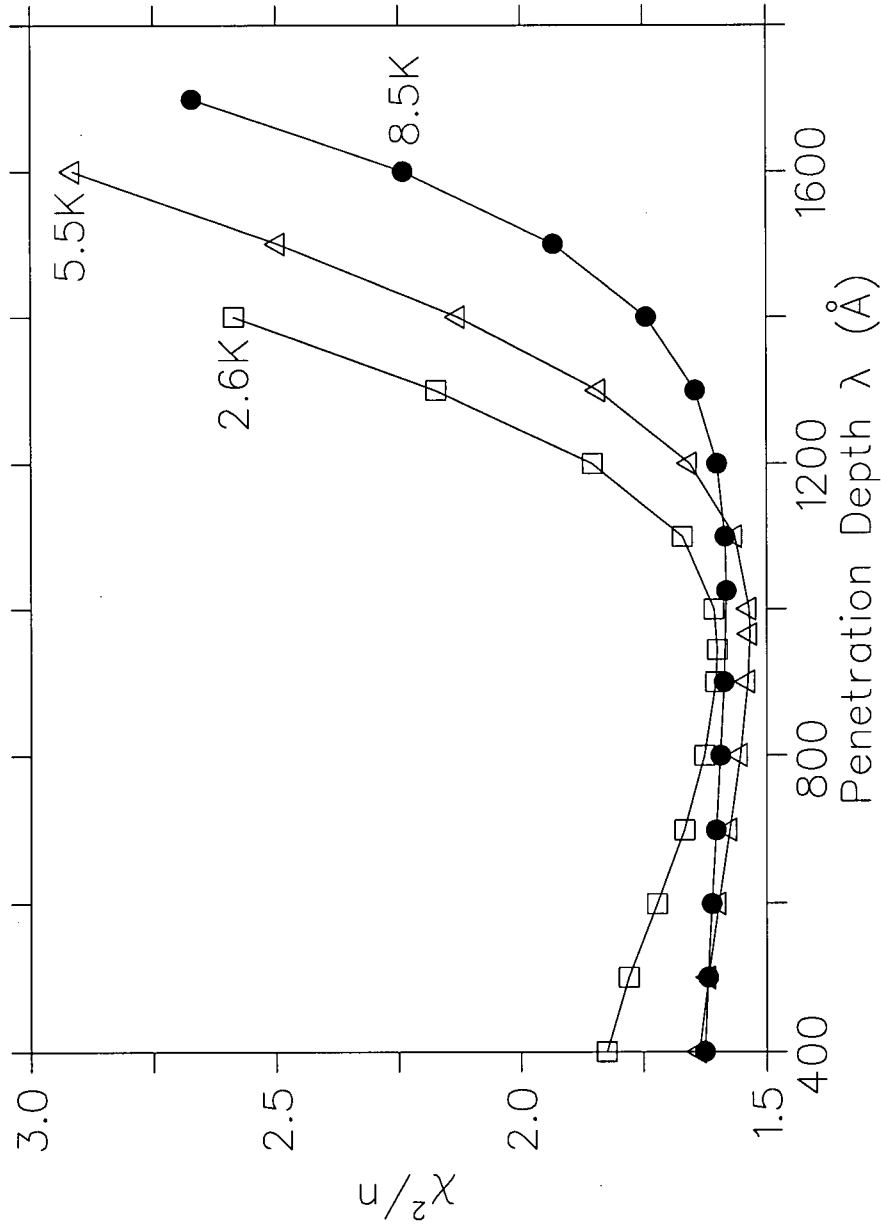


Figure 5.6: Reduced chi-squared χ^2/n as a function of penetration depth λ at temperatures $T = 2.6$ K (squares), $T = 5.5$ K (triangles) and $T = 8.5$ K (circles) under an applied field $H = 1.2$ T. Lines connect the χ^2/n points at each temperature T . The number of degrees of freedom n for each temperature T appears in Table 5.1.

Table 5.1: Number of data points n analysed at each temperature T in Figures 5.6, 5.7 and 5.8.

Temperature T (K)	Number of data points n
2.6	556
5.5	550
8.5	547

parameters, especially the nonlocality parameter C . Parameter C drops monotonically by two to three orders of magnitude over the displayed interval of increasing penetration depth λ . This substantial payoff comes from the factor $\lambda^4 C$ appearing in the internal spatial field profile (5.2). The widening minima at higher temperatures T reflects the diminishing asymmetry of the internal field distribution $n(B)$ as it approaches a Gaussian form. Figure 5.7 reveals how χ^2/n varies with the nonlocality parameter C . At each temperature χ^2/n grows rapidly as C decreases below the location of the minimum χ^2/n . This clearly demonstrates the substantial improvement in fit quality achieved by incorporating nonlocal corrections into the London model. The slow growth in χ^2/n as the nonlocality parameter C increases away from the minimum further evidences the payoff between C and the penetration depth λ . The penetration depth λ falls monotonically as the nonlocality parameter C rises over the plotted interval. The shallower minima at warmer temperatures T again stem from the more Gaussian-like internal field distribution $n(B)$. Figure 5.8 displays χ^2/n for a range of vortex core radii ρ at the same temperatures T . Since the core radius ρ is a calculated rather than fitted parameter, this graph is constructed by minimising χ^2 at fixed values of the coherence length ξ and noting the corresponding core radii ρ . The strongly linear relationship between the coherence length ξ and the core radius ρ makes this process possible. Similarly, altering the coherence length ξ by its uncertainty $\delta\xi$ and observing the consequent change in the core radius ρ produces error bars $\delta\rho$ for the core radius ρ . This means of computation of the uncertainty $\delta\rho$ in the core radius ρ is far simpler and more tractable than one based on combining the uncertainties of the fitted parameters according to equations (5.2) and (5.10). At each temperature T the χ^2/n curve has a single minimum, which moves to larger core radii ρ as the temperature T rises. This behaviour of the core radius ρ , and also the penetration depth λ , with temperature T is explored in more detail in the next chapter.

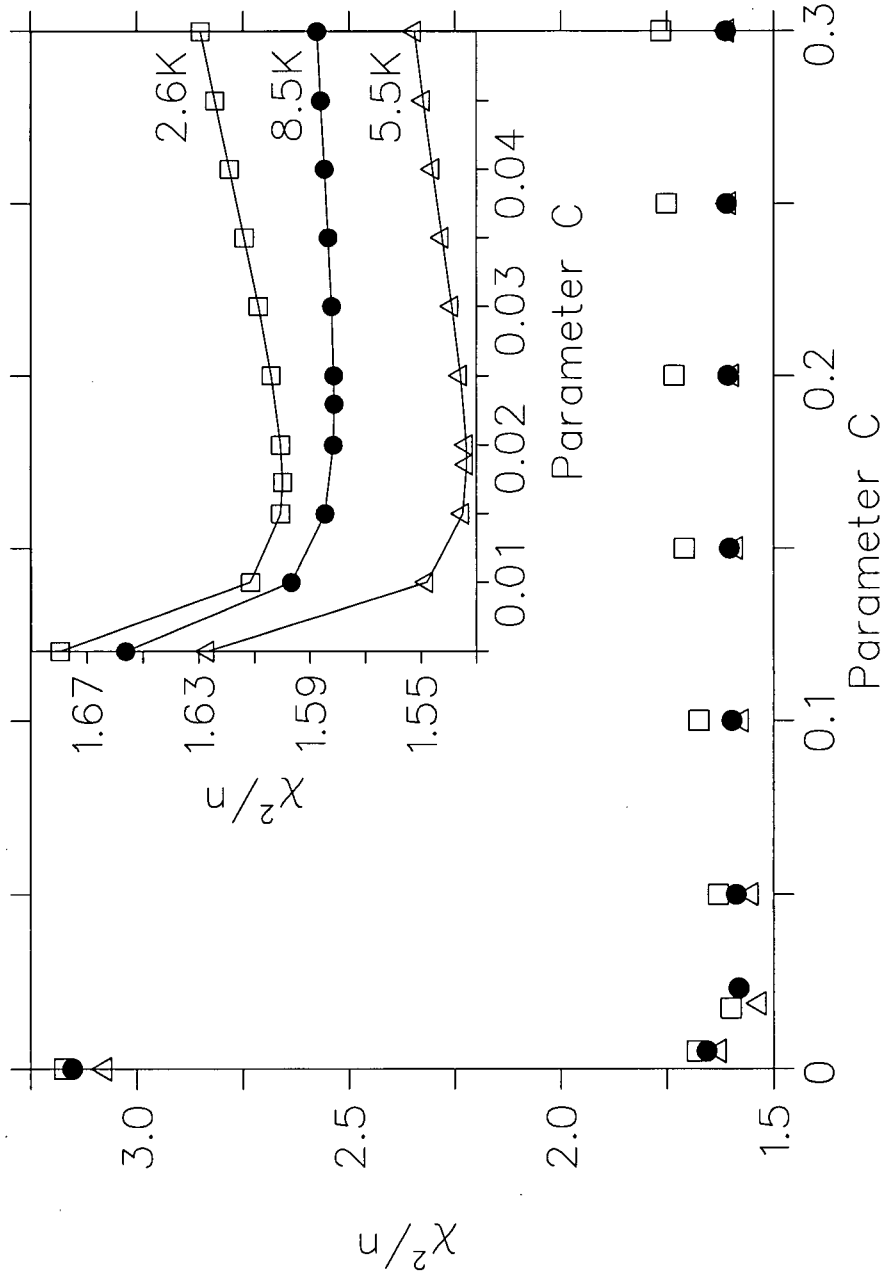


Figure 5.7: Reduced chi-squared χ^2/n as a function of nonlocality parameter C at temperatures $T = 2.6$ K (squares), $T = 5.5$ K (triangles) and $T = 8.5$ K (circles) under an applied field $H = 1.2$ T. Inset: Magnified view of χ^2/n minima. Lines connect the χ^2/n points at each temperature T . The number of degrees of freedom n for each temperature T appears in Table 5.1.

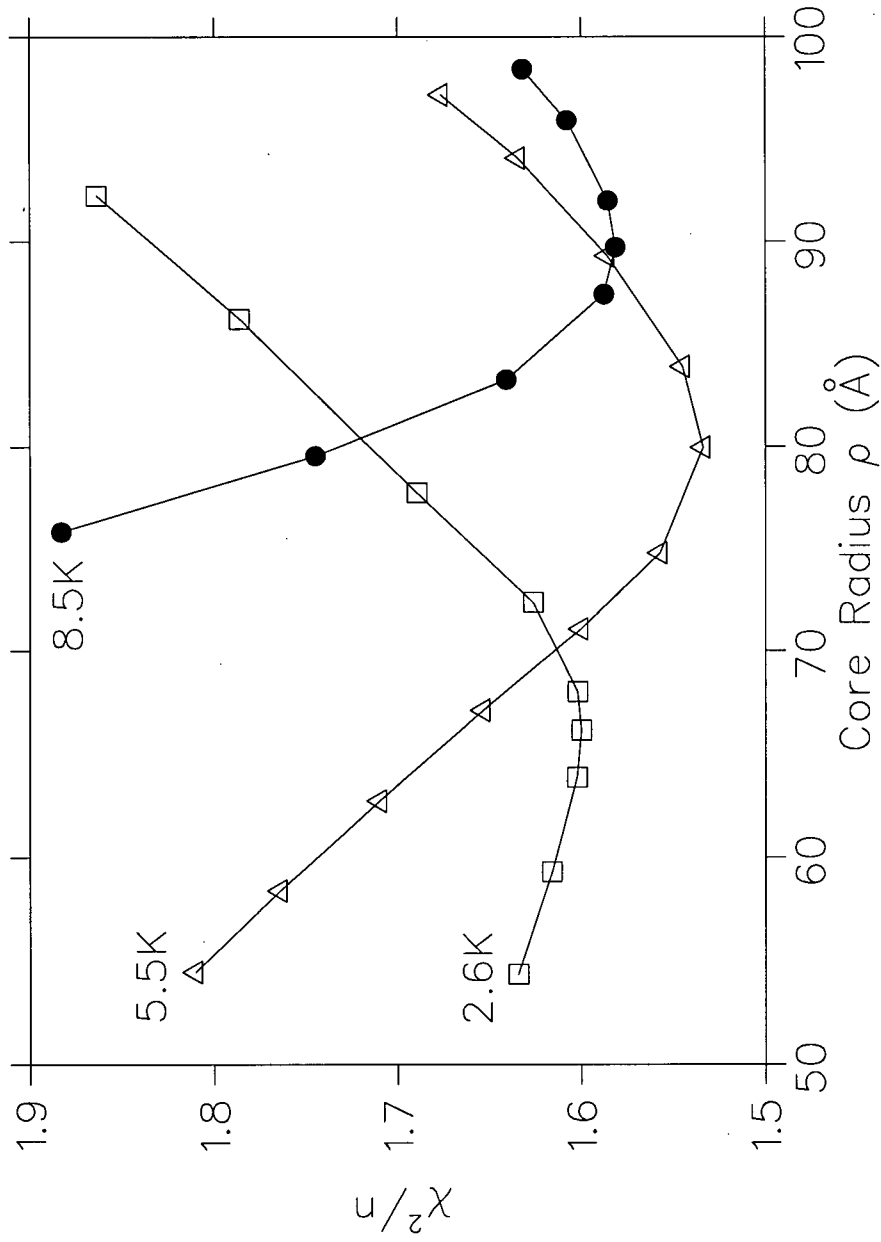


Figure 5.8: Reduced chi-squared χ^2/n and core radius ρ at temperatures $T = 2.6$ K (squares), $T = 5.5$ K (triangles) and $T = 8.5$ K (circles) under an applied field $H = 1.2$ T. Lines connect the χ^2/n points at each temperature T . The number of degrees of freedom n for each temperature T appears in Table 5.1.

Chapter 6

Results and Discussion

The nonlocal model outlined in Section 5.2 fitted the μ SR data on $\text{LuNi}_2\text{B}_2\text{C}$ much better than the local London model used in combination with a triangular vortex lattice [51]. This reflects the presence of a highly ordered square flux lattice in $\text{LuNi}_2\text{B}_2\text{C}$ at temperatures T between $T = 2.6$ K and $T = 10$ K, achieved through field cooling under an $H = 1.2$ T field applied parallel to the crystal \hat{c} axis. The behaviour of the penetration depth λ , the nonlocality parameter C and the core radius ρ in $\text{LuNi}_2\text{B}_2\text{C}$ under these field and temperature conditions emerges readily from the fitted parameters.

Figure 6.1(a) displays the behaviour of the fitted penetration depth λ with temperature T under an external field $H = 1.2$ T. The fitted penetration depth λ increases from $\lambda \approx 950$ Å to $\lambda \approx 1100$ Å over the temperature T range from $T = 2.6$ K to $T = 10$ K. The solid curve depicts the temperature dependence anticipated from relation (5.4) and plotted in Figure 5.1. Choosing a zero temperature penetration depth $\lambda(0)$ to optimally fit this BCS temperature variation to the measured penetration depth λ indicates a zero temperature penetration depth $\lambda(0) = 949(8)$ Å. The observed penetration depth appears fairly consistent with the exponentially-activated form expected for BCS electron-phonon coupling and s -wave order parameter symmetry in $\text{LuNi}_2\text{B}_2\text{C}$. However, the error bar size also permits the interpretation of the penetration depth temperature dependence $\lambda(T)$ as a power law; as would be expected [7] if nodes existed in the energy gap. The penetration depth grows much more weakly with temperature in $\text{LuNi}_2\text{B}_2\text{C}$ than in $\text{YBa}_2\text{Cu}_3\text{O}_{6.95}$ [52], known to possess an energy gap with line nodes. While the penetration depth λ measurements seem as anticipated, the fitted nonlocality parameter C appears a little more surprising.

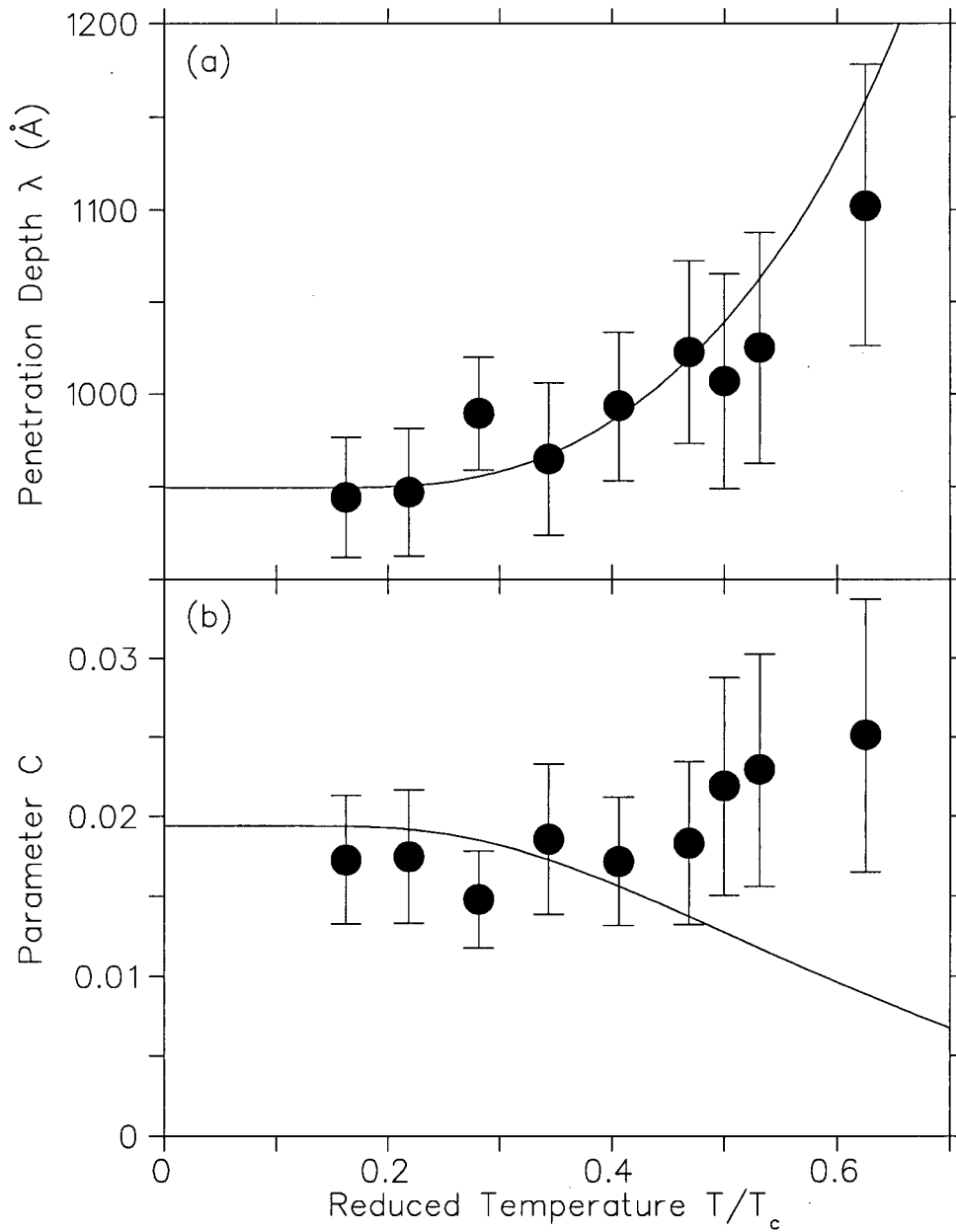


Figure 6.1: Measured dependence of (a) the penetration depth λ and (b) the nonlocality parameter C on temperature T in $\text{LuNi}_2\text{B}_2\text{C}$ under an applied field $H = 1.2\text{ T}$. The circles are the best fit values obtained with the nonlocal London model. For comparison, the solid lines illustrate the expected variation according to (a) expression (5.4) and (b) relation (5.3).

Figure 6.1(b) depicts the variation of the fitted nonlocality parameter C with temperature T under an $H = 1.2$ T applied field. As described in Section 5.5, reasonable fits to the data require a nonzero C , demonstrating the importance of nonlocal effects in $\text{LuNi}_2\text{B}_2\text{C}$. The solid curve in Figure 6.1(b) is a fit to the predicted temperature dependence (5.3) in the clean limit. As expected, the best fit values of the nonlocality parameter C are fairly uniform at low temperatures. At higher temperatures the fitted nonlocality parameter C changes little, rather than dropping monotonically as anticipated. Possible explanations for this slight discrepancy include the presence of impurities and the approximate nature of the field distribution model (5.2). Figure 5.1 illustrates the behaviour of parameter C with temperature, as influenced by the nonlocality radius ρ_{nl} , when the $\text{LuNi}_2\text{B}_2\text{C}$ sample is completely free of impurities. As the impurity level rises the nonlocality radius ρ_{nl} becomes temperature independent [12], leading to a weaker temperature dependence in parameter C that better agrees with that observed. In fact, the constancy of the fitted nonlocality parameter C over the studied temperature range agrees with recent small angle neutron scattering (SANS) data [53] that shows the onset field H_2 of the square to hexagonal vortex lattice symmetry transition essentially holds constant below temperature $T = 10$ K. Closer agreement between the anticipated and fitted temperature dependences of parameter C might also result from the inclusion of higher order nonlocal terms in expression (5.2) for the spatial field profile $\mathbf{B}(r)$. Refitting the data with the nonlocality parameter C fixed to its expected clean limit temperature variation (5.3) induces negligible change in the remaining fitted parameters and the inferred core radius ρ .

Table 6.1: Fitted penetration depth λ , effective coherence length ξ and nonlocality parameter C for the field distributions $n(B)$ plotted in Figure 6.2.

London model	Temperature T (K)	λ (Å)	ξ (Å)	C
Nonlocal	10	1100(80)	57(1)	0.25(9)
Nonlocal	2.6	940(30)	28(2)	0.17(4)
Local	2.6	1494(9)	41(1)	0

Figure 6.2 compares the internal magnetic field distributions $n(B)$ calculated for the fitted spatial field profile (5.2) at temperatures $T = 2.6$ K and $T = 10$ K under an $H = 1.2$ T external field. The best fit values of the penetration depth λ , the effective coherence length ξ and the nonlocality parameter C for the distributions $n(B)$ shown in this figure appear in Table 6.1. The shape of the

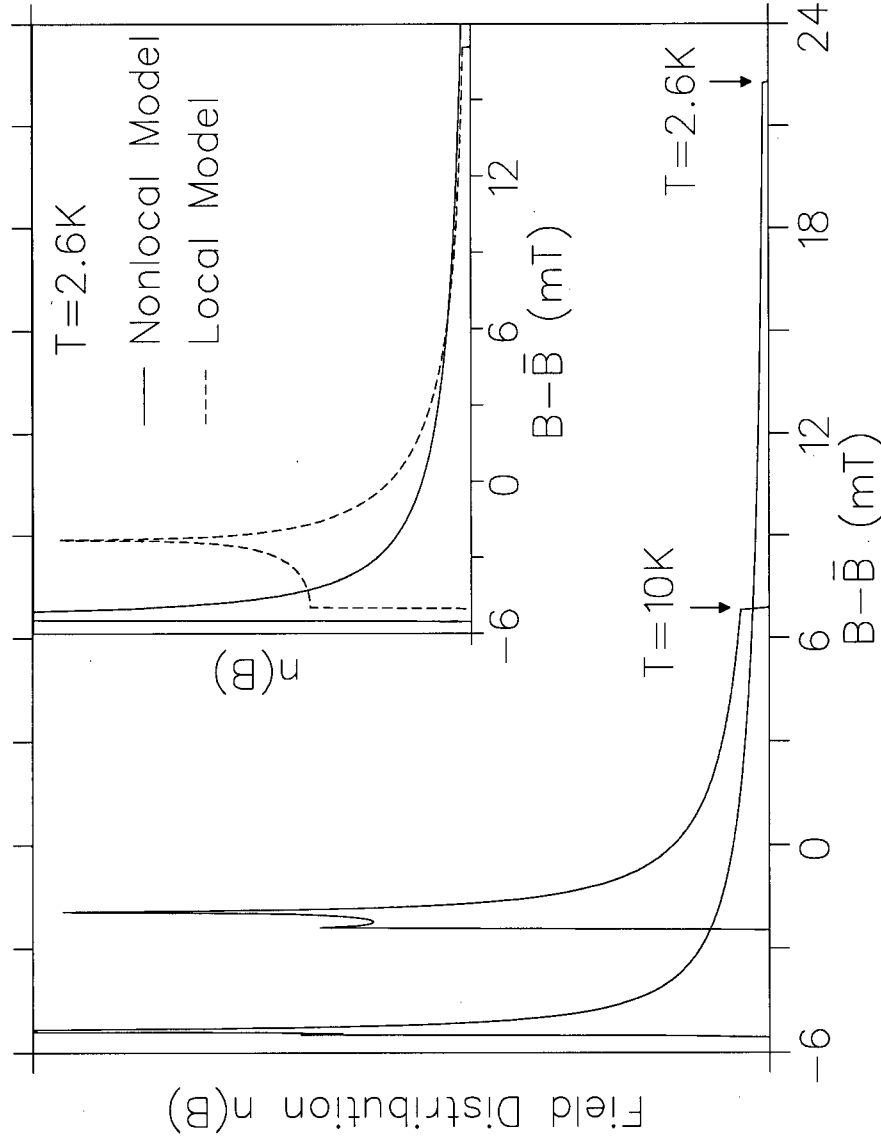


Figure 6.2: Fitted internal magnetic field distribution $n(B)$ at temperatures $T = 2.6\text{ K}$ and $T = 10\text{ K}$ under an applied field $H = 1.2\text{ T}$. The internal field B is shown relative to its average \bar{B} . At both temperatures an arrow highlights the maximum field, located at the centre of a vortex core. Inset: Field distributions $n(B)$ belonging to the best fit at $T = 2.6\text{ K}$ for the nonlocal London model (5.2) (solid line) and the traditional London model (dashed line) obtained by setting the parameter C to zero.

nonlocal field distributions $n(B)$ differs qualitatively from that associated with the traditional London model, as illustrated at temperature $T = 2.6$ K in the inset to this figure. The distinct difference between these shapes explains the vast improvement in fit quality the nonlocal London model (5.2) achieves over the conventional one, as evident in Figure 5.7. The basic London model emerges from the nonlocal model when the nonlocality parameter $C = 0$, and, in the case of a square vortex lattice, generates a characteristic low field shoulder in the field distribution $n(B)$. The nonlocal corrections greatly reduce the spectral weight of this shoulder, to the point where at temperature $T = 2.6$ K the shoulder almost vanishes. They also give rise to the small peak appearing at the lowest field B in the distribution $n(B)$. Such a peak is absent in the local London model, and its presence reflects a flatter spatial field profile at the centre of the square unit cell with a vortex in each corner. The clear rise in the maximum field B of the distribution $n(B)$ as the temperature T falls from $T = 10$ K to $T = 2.6$ K reflects the shortening of the vortex core radius ρ .

Figure 6.3 compares the temperature dependence of the core radius $\rho(T)$ measured in $\text{LuNi}_2\text{B}_2\text{C}$ at external field $H = 1.2$ T to that reported for NbSe_2 [6] ($T_c = 7.0$ K), $\text{YBaCu}_3\text{O}_{6.95}$ [7] ($T_c = 93.2$ K) and $\text{YBaCu}_3\text{O}_{6.60}$ ($T_c = 59$ K) at $H = 0.5$ T. As the reduced temperature T/T_c rises from $T/T_c = 0$ to $T/T_c \approx 0.6$, the core radius ρ in $\text{YBaCu}_3\text{O}_{6.95}$ and $\text{YBaCu}_3\text{O}_{6.60}$ remains almost constant, consistent with the attainment of the quantum limit as discussed in Section 2.4. In NbSe_2 the quantum limit temperature T_0 occurs around 1 K, above which the core radius ρ expands linearly with temperature T , at a rate much slower than anticipated from the proposed Kramer-Pesch effect. The Kramer-Pesch effect in $\text{LuNi}_2\text{B}_2\text{C}$ appears equally weak, with no low temperature saturation in its core size evident over the temperature interval studied. Overlapping the $\text{LuNi}_2\text{B}_2\text{C}$ data with that for NbSe_2 determines the zero temperature core radius $\rho(0)$ for $\text{LuNi}_2\text{B}_2\text{C}$ to be $\rho(0) = 64(1)$ Å, greatly exceeding the predicted value $\rho(0) \sim 1/k_F = 4$ Å. The relation $\rho = \rho(0)[1 + \alpha(T - T_0)/T_c]$, displayed as a solid line in Figure 6.3 with the zero temperature core radius $\rho(0)$ set to 64 Å, best fits the $\text{LuNi}_2\text{B}_2\text{C}$ data for slope $\alpha = 0.84(5)$ and quantum limit temperature $T_0 = 1.0(4)$ K. This agrees with the expected quantum limit temperature $T_0 = 0.7(1)$ K calculated in Section 3.2, and is similar to that recorded for NbSe_2 . The almost identical reduced temperature T/T_c dependence of the core radius $\rho/\rho(0)$ in $\text{LuNi}_2\text{B}_2\text{C}$ and NbSe_2 suggests that quasiparticles in these materials behave in the same way as a function of reduced temperature T/T_c , despite the different dimensionalities of these superconductors. It also implies that longitudinal disorder of vortices has negligible effect on μSR determinations of the core radius ρ . As with μSR studies of the Kramer-Pesch effect in NbSe_2 and $\text{YBaCu}_3\text{O}_{7-\delta}$, the weak core shrinkage upon

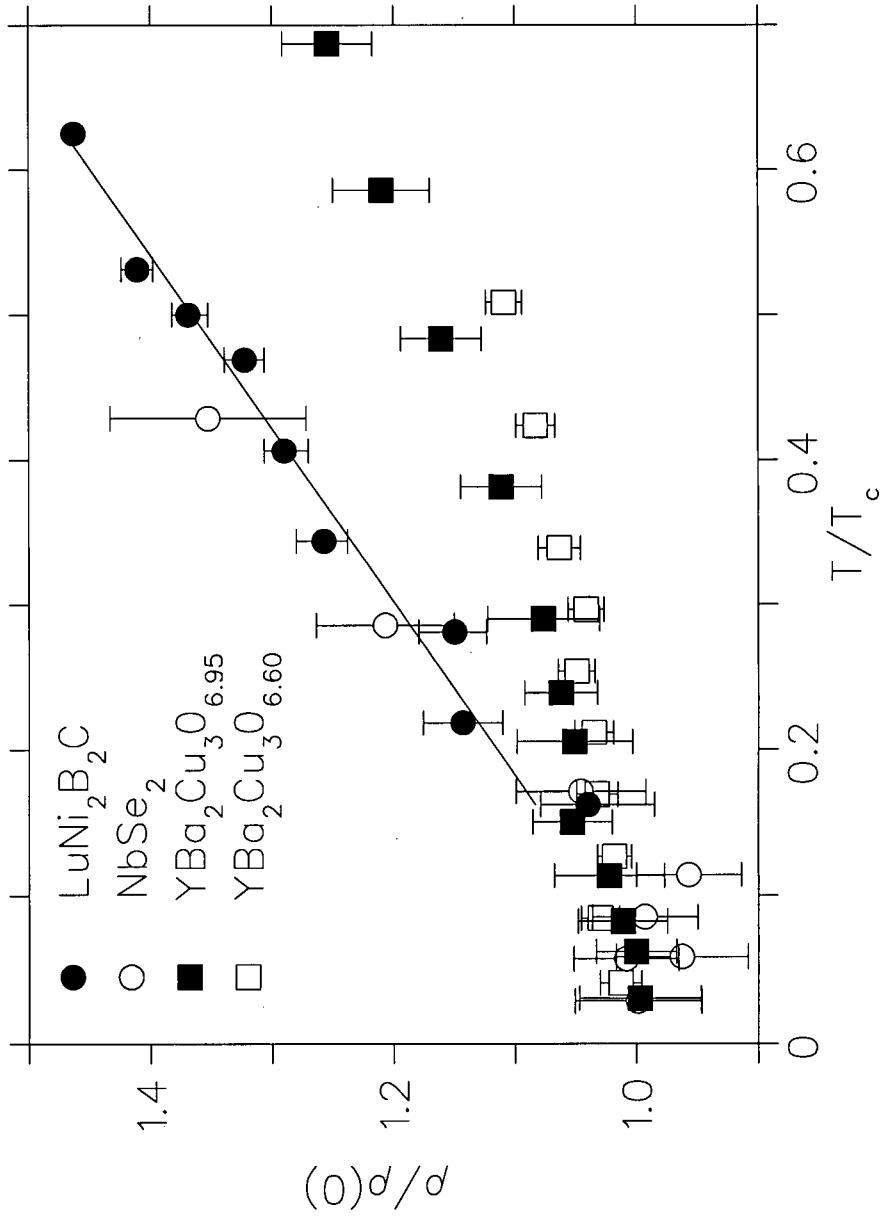


Figure 6.3: Behaviour of the core radius ρ with temperature T in $\text{LuNi}_2\text{B}_2\text{C}$ ($T_c = 16.0$ K, solid circles), NbSe_2 [6] ($T_c = 7.0$ K, open circles), $\text{YBaCu}_3\text{O}_{6.95}$ [7] ($T_c = 93.2$ K, solid squares) and $\text{YBaCu}_3\text{O}_{6.60}$ ($T_c = 59$ K, open squares) at applied fields of $H = 1.2$ T ($\text{LuNi}_2\text{B}_2\text{C}$) and $H = 0.5$ T (NbSe_2 and $\text{YBaCu}_3\text{O}_{7-\delta}$). The solid line $\rho/\rho(0) = 1 + \alpha(T - T_0)/T_c$ is a fit to the $\text{LuNi}_2\text{B}_2\text{C}$ data with $\alpha = 0.84(5)$ and $T_0 = 1.0(4)$ K.

cooling and order-of-magnitude larger than expected zero temperature core radius $\rho(0)$ observed in $\text{LuNi}_2\text{B}_2\text{C}$ highlight the need to include interactions between vortices and their zero point motion in theories concerning the Kramer-Pesch effect.

Chapter 7

Conclusions

This thesis reports μ SR measurements of the internal magnetic field distribution $n(B)$ in $\text{LuNi}_2\text{B}_2\text{C}$ at temperatures T between $T = 2.6$ K and $T = 10$ K, under a magnetic field $H = 1.2$ T applied parallel to the crystal c axis. The μ SR data are analysed with a nonlocal London model [11] developed specifically for borocarbide superconductors, assuming the square vortex lattice appropriate for these temperature T and external field H conditions. The results of this analysis enable a number of conclusions to be drawn regarding nonlocality and the behaviour of the penetration depth λ and core radius ρ with temperature T in $\text{LuNi}_2\text{B}_2\text{C}$.

Nonlocality plays an important role in the vortex state of $\text{LuNi}_2\text{B}_2\text{C}$. The incorporation of first order nonlocal corrections into the traditional London model improves the fit quality dramatically by qualitatively modifying the fitted internal magnetic field distribution $n(B)$. In comparison to the field distribution $n(B)$ produced for a square vortex lattice by the basic London model, the inclusion of these nonlocal terms considerably diminishes the spectral weight of the low field shoulder and generates a small peak at the lowest field B in the distribution $n(B)$.

The penetration depth λ in $\text{LuNi}_2\text{B}_2\text{C}$ increases slightly from $\lambda \approx 950$ Å at temperature $T = 2.6$ K to $\lambda \approx 1100$ Å at $T = 10$ K. The form of the measured penetration depth temperature variation $\lambda(T)$ agrees with that expected for a BCS s -wave superconductor, although the error bars suffice in size for the observed temperature dependence $\lambda(T)$ to be consistent with weak linear growth. Such a linear rise in the penetration depth λ at low temperatures would imply the presence of low energy delocalised quasiparticles. However the considerably reduced steepness of the possible linear growth in $\text{LuNi}_2\text{B}_2\text{C}$ relative to that observed for

$\text{YBa}_2\text{Cu}_3\text{O}_{6.95}$ means that the energy gap Δ anisotropy in $\text{LuNi}_2\text{B}_2\text{C}$ is much less than would be generated by line nodes.

The core radius ρ in $\text{LuNi}_2\text{B}_2\text{C}$ contracts linearly upon cooling through the investigated temperature interval. The rate of core shrinkage is remarkably slower than anticipated from the predicted Kramer-Pesch effect. The zero temperature core radius $\rho(0) = 64(1) \text{ \AA}$, as determined by comparison with NbSe_2 data, greatly exceeds the proposed $\rho(0) \sim 1/k_F = 4 \text{ \AA}$. However, the extrapolated quantum limit temperature $T_0 = 1.0(4) \text{ K}$ for $\text{LuNi}_2\text{B}_2\text{C}$ agrees well with the expected value $T_0 = 0.7(1) \text{ K}$. Surprisingly, the behaviour of the core radius $\rho/\rho(0)$ with reduced temperature T/T_c is almost identical in nearly three-dimensional $\text{LuNi}_2\text{B}_2\text{C}$ and quasi two-dimensional NbSe_2 . This similarity indicates that longitudinal disorder of vortices exerts negligible influence on μSR measurements of the vortex core radius ρ , and that quasiparticles in these two superconductors act in much the same manner. As is the case for NbSe_2 , the weakness of the observed Kramer-Pesch effect in $\text{LuNi}_2\text{B}_2\text{C}$ points to the need for theoretical work on the temperature dependence of vortex structure to take into account zero point motion of vortices and vortex-vortex interactions.

Bibliography

- [1] M. Tinkham, *Introduction to Superconductivity* 2nd ed. (MacGraw-Hill, Inc., New York, ch. 4, 1996).
- [2] A. N. Price, R. I. Miller, R. F. Kiefl, J. A. Chakhalian, S. R. Dunsiger, G. D. Morris, J. E. Sonier and P. C. Canfield (unpublished).
- [3] L. Kramer and W. Pesch, *Z. Physik* **269**, 59 (1974).
- [4] F. Gygi and M. Schlüter, *Phys. Rev. B* **43**, 7609 (1991).
- [5] N. Hayashi, T. Isoshima, M. Ichioka and K. Machida, *Phys. Rev Lett.* **80**, 2921 (1998).
- [6] R. I. Miller, R. F. Kiefl, J. H. Brewer, J. Chakhalian, S. Dunsiger, G. D. Morris, J. E. Sonier and W. A. MacFarlane, *Phys. Rev Lett.* **85**, 1540 (2000).
- [7] J. E. Sonier, J. H. Brewer and R. F. Kiefl, *Rev. Mod. Phys.* **72**, 769 (2000).
- [8] M. Tinkham, *Introduction to Superconductivity* 2nd ed. (MacGraw-Hill, Inc., New York, ch. 1, 1996).
- [9] D. Saint-James, G. Sarma and E. J. Thomas, *Type II Superconductivity* (Pergamon, Oxford, pp. 64-65, 1969).
- [10] V. G. Kogan, P. Miranović, Lj. Dobrasavljević-Grujić, W. E. Pickett and D. K. Christen, *Phys. Rev. Lett.* **79**, 741 (1997).
- [11] V. G. Kogan, M. Bullock, B. Harmon, P. Miranović, Lj. Dobrasavljević-Grujić, P. L. Gammel and D. J. Bishop, *Phys. Rev. B* **55**, R8693 (1997).
- [12] V. G. Kogan, A. Gurevish, J. H. Cho, D. C. Johnston, M. Xu, J. R. Thompson and A. Martynovich, *Phys. Rev. B* **54**, 12386 (1996).

- [13] M. Tinkham, *Introduction to Superconductivity* 2nd ed. (MacGraw-Hill, Inc., New York, ch. 3, 1996).
- [14] A. C. Rose-Innes and E. H. Rhoderick, *Introduction to Superconductivity* 2nd ed. (Pergamon, Oxford, ch. 9, 1978).
- [15] J. Bardeen, L. N. Cooper and J. R. Schrieffer, *Phys. Rev.* **108**, 1175 (1957).
- [16] M. Tinkham, *Introduction to Superconductivity* 2nd ed. (MacGraw-Hill, Inc., New York, ch. 9, 1996).
- [17] V. Z. Kresin and S. A. Wolf, *Fundamentals of Superconductivity* (Plenum, New York, p. 33, 1990).
- [18] V. Z. Kresin and S. A. Wolf, *Fundamentals of Superconductivity* (Plenum, New York, pp. 21-22, 1990).
- [19] D. Saint-James, G. Sarma and E. J. Thomas, *Type II Superconductivity* (Pergamon, Oxford, pp. 22-25, 1969).
- [20] C. Caroli, P. G. de Gennes and J. Matricon, *Phys. Lett.* **9**, 307 (1964).
- [21] S. G. Doettinger, R. P. Huebener and S. Kittelberger, *Phys. Rev. B* **55**, 6044 (1997).
- [22] W. Pesch and L. Kramer, *J. Low Temp. Physics* **15**, 367 (1974).
- [23] S. G. Doettinger, S. Anders, R. P. Huebener, H. Haensel and Yu. N. Ovchinnikov, *Europhys. Lett. B* **30**, 549 (1995).
- [24] J. E. Sonier, R. F. Kiefl, J. H. Brewer, D. A. Bonn, S. R. Dunsiger, W. N. Hardy, R. Liang, R. I. Miller, D. R. Noakes and C. E. Stronach, *Phys. Rev. B* **59**, R729 (1999).
- [25] J. E. Sonier, J. H. Brewer, R. F. Kiefl, D. A. Bonn, S. R. Dunsiger, W. N. Hardy, R. Liang, W. A. MacFarlane, R. I. Miller, T. M. Riseman, D. R. Noakes, C. E. Stronach and M. F. White, *Phys. Rev Lett.* **79**, 2875 (1997).
- [26] J. W. Lynn, S. Skanthakumar, Q. Huang, S. K. Sinha, Z. Hossain, L. C. Gupta, R. Nagarajan and C. Godart, *Phys. Rev. B* **55** 6584, (1997).

- [27] S. L. Drechsler, S. V. Shulga, K. H. Müller, G. Fuchs, J. Freudenberger, G. Behr, H. Eschrig, L. Schultz, M. S. Golden, H. von Lips, J. Fink, V. H. Narozhnyi, H. Rosner, P. Zahn, A. Gladun, D. Lipp, A. Kreyssig, M. Loewenhaupt, K. Kopernik, K. Winzer and K. Krug, *Physica C* **317-318**, 117 (1999).
- [28] I. R. Fisher, J. R. Cooper and P. C. Canfield, *Phys. Rev. B* **56**, 10820 (1997).
- [29] H. Takagi, M. Nohara and C. Cava, *Physica B* **237-238**, 292 (1997).
- [30] P. L. Gammel, D. Lopez, D. J. Bishop, M. R. Eskildsen, N. H. Anderson, K. Mortensen, I. R. Fisher, K. O. Cheon and P. C. Canfield, *J. Appl. Phys.* **87**, 5544 (2000).
- [31] M. Yethiraj, H. Kawano, D. McK. Paul, C. V. Tomy, H. Takeya, H. Yoshizawa, *Journal of Physics and Chemistry of Solids* **60**, 1059 (1999).
- [32] L. C. Gupta, *Philosophical Magazine B* **77**, 717 (1998).
- [33] P. C. Canfield, P. L. Gammel and D. J. Bishop, *Physics Today* **October**, 40 (1998).
- [34] S. B. Dugdale, M. A. Alam, I. Wilkinson, R. J. Hughes, I. R. Fisher, P. C. Canfield, T. Jarlborg and G. Santi, *Phys. Rev. Lett.* **83**, 4824 (1999).
- [35] T. Siegrist, H. W. Zandbergen, R. J. Cava, J. J. Krajewski and W. F. Peck Jr, *Nature* **367**, 254 (1994).
- [36] W. E. Pickett and D. J. Singh, *Phys. Rev. Lett.* **72**, 3702 (1994).
- [37] V. Metlushko, U. Welp, A. Koshelev, I. Aranson, G. W. Crabtree and P. C. Canfield, *Phys. Rev. Lett.* **79**, 1738 (1997).
- [38] H. Michor, T. Holubar, C. Dusek and G. Hilscher, *Phys. Rev. B* **52**, 16165 (1995).
- [39] S. V. Shulga, S. L. Drechsler, G. Fuchs, K. H. Müller, K. Winzer, M. Heinecke and K. Krug, *Phys. Rev. Lett.* **80**, 1730 (1998).
- [40] J. F. Annett, *Physica C* **317-318**, 1 (1999).
- [41] Y. DeWilde, M. Iavarone, U. Welp, V. Metlushko, A. E. Koshelev, I. Aranson, G. W. Crabtree and P. C. Canfield, *Phys. Rev. Lett.* **78**, 4273 (1997).

- [42] E. Boaknin, R. W. Hill, C. Proust, C. Lupien, L. Taillefer and P. C. Canfield, cond-mat/0012436.
- [43] M. R. Eskildsen, P. L. Gammel, B. P. Barber, A. P. Ramirez, D. J. Bishop, N. H. Andersen, K. Mortensen, C. A. Bolle, C. M. Lieber and P. C. Canfield, Phys. Rev. Lett. **79**, 487 (1997).
- [44] L. Ya. Vinnikov, T. L. Barkov, K. O. Cheon, P. C. Canfield and V. G. Kogan, Physica B **284-288**, 813 (2000).
- [45] L. Ya. Vinnikov, T. L. Barkov, P. C. Canfield, S. L. Bud'ko and V. G. Kogan, Phys. Rev. B **64**, 024504 (2001).
- [46] M. R. Eskildsen, A. B. Abrahamsen, D. López, P. L. Gammel, D. J. Bishop, N. H. Andersen, K. Mortensen and P. C. Canfield, Phys. Rev. Lett. **86**, 320 (2001).
- [47] B. K. Cho, P. C. Canfield, L. L. Miller, D. C. Johnston, W. P. Beyermann and A. Yatskar, Phys. Rev. B **52**, 3684 (1995).
- [48] K. O. Cheon, I. R. Fisher, V. G. Kogan, P. C. Canfield, P. Miranović and P. L. Gammel, Phys. Rev. B **58**, 6463 (1998).
- [49] J. E. Sonier, Ph. D. thesis, University of British Columbia (1998).
- [50] A. Yaouanc, P. Dalmas de Réotier and E. H. Brandt, Phys. Rev. B **55**, 11107 (1997).
- [51] R. I. Miller, private communication.
- [52] J. E. Sonier, R. F. Kiefl, J. H. Brewer, D. A. Bonn, S. R. Dunsiger, W. N. Hardy, R. Liang, W. A. MacFarlane and T. M. Riseman, Phys. Rev. B **55**, 11789 (1997).
- [53] M. R. Eskildsen, A. B. Abrahamsen, V. G. Kogan, P. L. Gammel, K. Mortensen, N. H. Andersen and P. C. Canfield, Phys. Rev. Lett. **86**, 5148 (2001).